The 29 June 2000 Supercell Observed during STEPS.
Part I: Kinematics and Microphysics

Sarah A. Tessendorf

Department of Atmospheric Science, Colorado State University, Fort Collins, Colorado

L. Jay Miller

National Center for Atmospheric Research,* Boulder, Colorado

Kyle C. Wiens[+] and Steven A. Rutledge

Department of Atmospheric Science, Colorado State University, Fort Collins, Colorado

ABSTRACT

This is a two-part study that addresses the kinematic, microphysical, and electrical aspects of a severe storm that occurred in western Kansas on 29 June 2000 observed during the Severe Thunderstorm Electrification and Precipitation Study (STEPS) field campaign. In this first part, polarimetric and Doppler radar data are used along with a simple particle growth model to examine the evolution of the kinematic and microphysical properties of the storm from its earliest developing phase through its mature and dissipating phases. During its severe stage, the storm exhibited frequent positive cloud-to-ground lightning strikes, very large ($\sim$5 cm) hail, and a tornado.

Doppler-derived winds, radar reflectivity, and hydrometeor classifications from the polarimetric data over a nearly 4-h period are presented. It is shown that updraft velocity and vertical vorticity had to reach magnitudes of at least 10 m s^{-1} and 10^{-2} s^{-1} and occupy major portions of the storm before it could produce most of the observed severe storm characteristics. Furthermore, the establishment of cyclonic horizontal flow around the right flank of the updraft core was essential for hail production. Most of the largest hail grew from near millimeter-sized particles that originated in the mid- to upper-level stagnation region that resulted from obstacle-like flow of environmental air around the divergent outflow from the upper part of the updraft. These recycling embryonic particles descended around the right flank of the updraft core and reentered the updraft, intermingling with other smaller particles that had grown from cloud base along the main low-level updraft stream.

1. Introduction

The Severe Thunderstorm Electrification and Precipitation Study (STEPS) was established "to achieve a better understanding of the interactions between kinematics, precipitation production, and electrification in severe thunderstorms on the High Plains" (Weisman and Miller 2000). The field campaign took place from 17 May to 20 July 2000 near Goodland, Kansas. An overview of the STEPS field program can be found in Lang et al. (2004).

STEPS research aims to identify relationships between microphysical and dynamical processes in severe storms on the High Plains and, in particular, why some storms produce predominantly positive cloud-to-ground (PPCG) lightning. One specific scientific goal of STEPS, as outlined in the Scientific Overview (available online at http://www.mmm.ucar.edu/pdas/steps-science.html), is "to understand the formation of precipitation and its influence on electrical development,

---

Corresponding author address: Sarah A. Tessendorf, Dept. of Atmospheric Science, Colorado State University, Fort Collins, CO 80523.
E-mail: saraht@atmos.colostate.edu

especially in those storms producing large hail." In this first part of our two-part study, we will focus primarily on the evolutionary aspects of convective kinematics that ultimately lead to severe, hail-producing storms.

On 29 June 2000, a multicellular convective storm developed near Bird City, Kansas, and intensified into a supercell as it passed through the STEPS radar network between 2130 UTC 29 June and 0115 UTC 30 June.[1] This storm produced copious amounts of large hail (up to 5 cm), an F1 tornado, as well as extraordinary intracloud (IC) flash rates ($\sim$300 min^{-1}; Williams 2001) and frequent positive cloud-to-ground (CG) lightning strikes. The unique observational platforms employed and the nearly four hours of continuous kinematic and microphysical observations permit us to add new insight to previous studies on hail growth in supercells, especially regarding evolution into the severe storm stage.

Previous studies of hailstorms have shown that supercells are responsible for much of the large hail over the High Plains (Browning 1977). Browning and Foote (1976, hereafter BF76) outlined a three-stage process for hail production in supercells. In the first stage, small particles (or embryos) grow during their initial ascent near the right flank of the main updraft. Secondly, some of these embryos circulate cyclonically around the forward flank of the main updraft as they descend. This branch forms what is referred to as the embryo curtain around the main updraft. Lastly, particles from the embryo curtain are able to enter the main updraft and grow into large hailstones in a single up-and-down path. Nelson (1983) concluded that, although a recycling process similar to that of the BF76 model was certainly likely, potential embryos had to be coming from a much broader region (an "embryo corridor") than the rather limited area of the BF76 embryo curtain. Several other studies (Dye et al. 1983; Miller et al. 1983, 1988, 1990) have found that, to serve as effective embryos for hail growth, particles entering the updraft must already be as large as 100 μm to 1 mm, thus implying that a recycling process must be taking place.

Microphysical and kinematic factors that influence hail growth during a storm's near-steady, severe stage were outlined in Nelson (1987, his Table 2). Among the list of microphysical factors that contribute to large hail are high values of supercooled liquid water and large embryos. Kinematic factors for large hail were listed as

light horizontal flow across the updraft, large contiguous updraft area (with mean updraft of 20–40 m s^{-1}), and favorable horizontal updraft gradients. Nelson argued that kinematic factors had a much greater influence on "extreme hailfall" events compared to any that might result from microphysical factors as proposed by Knight and Knight (1973). We will further address the relative importance of these two basic controls on whether or not a storm can and does produce hail.

Because most studies of hail growth such as those cited have used measurements from storms that are already in their severe phase, we are left with several unanswered questions, certainly less than satisfactory answers. We still do not have a clear understanding of the relative importance of microphysics and kinematics in the production of hail and the origin(s) of the starting embryonic particles for hail growth. Further, we have only a rudimentary understanding of the evolution from early convection into severe, hail-producing storms.

This two-part study aims to establish the nature of this storm's kinematic structure, its evolution into a severe stage with large hail, and how these factors may have affected its resulting electrification and lightning characteristics. The first part of the study uses synthesized wind fields from Doppler radar observations and particle growth trajectories to investigate the relationships between the kinematics and microphysics that characterize the 29 June 2000 storm over the course of its four-hour lifetime from its earliest development through its mature and dissipating phases. Additionally, we hope to better identify the coupling of kinematic and/or microphysical controls on large hail growth. Furthermore, the diagnosis of trajectories that favored graupel and hail growth in this storm will aid in our interpretation of how the kinematics and precipitation growth might have influenced the electrification processes discussed in Wiens et al. (2005, hereafter Part II). Part II uses the New Mexico Tech Lightning Mapping Array to infer the storm's total lightning and charge structure and to examine detailed observations of PPCG lightning in this storm and theories for its production.

2. Data and methods

Instrumentation and observing systems operated during the STEPS field campaign and used in this study include three S-band Doppler radars (two of which were polarimetric research radars) for mapping the three-dimensional structure of precipitation and storm winds; balloonborne in situ electric field mills to measure in-storm parameters including temperature, pres-

---

[1] All times are coordinated universal time (UTC); local time for this case study is found by subtracting six hours. All references to altitude will be in kilometers above mean sea level (MSL). The local ground level was approximately 1.1 km MSL. All listed particle sizes will be particle diameters.

TABLE 1. Characteristics of the radars used in this study.

Radar characteristic	CSU–CHILL	NCAR S-Pol	KGLD WSR-88D
Wavelength (cm)	11.01	10.71	10.0
Polarization	Linear, H and V	Linear, H and V	Linear, H
Peak power (kW)	800–1000	>1000	475
Beamwidth (deg)	1.1	0.91	1.0
Pulse repetition frequency (Hz)	1000	960	1000
Nyquist (m s^{-1})	27.5	25.7	25
Maximum range (km)	150	156.25	150

sure, wind, and electric field operated by the National Severe Storms Laboratory (NSSL) (Rust and MacGorman 2002); a mobile sounding unit for environmental wind and thermodynamic profiles near the storm; and the National Lightning Detection Network (NLDN) to measure CG lightning strike locations and polarities in "real time" (Cummins et al. 1998).

a. Basic radar data and derived winds

The Colorado State University (CSU)–University of Chicago and Illinois State Water Survey (CHILL) and National Center for Atmospheric Research (NCAR) S-band dual-polarization Doppler radars (S-Pol), along with the Goodland National Weather Service (NWS)
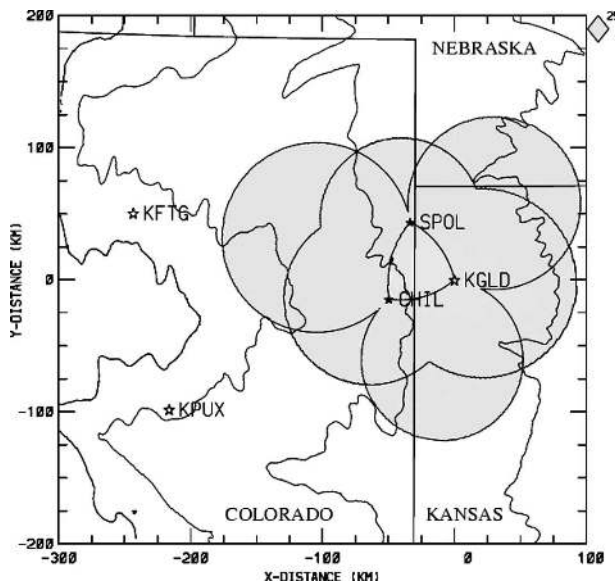

FIG. 1. Nominal areas of coverage (gray shading outlined with thick black lines) by the STEPS radar network (CHILL–S-Pol–KGLD) for dual-Doppler (beam-crossing angles between 25° and 155°) winds. Topographic height contours (black lines) are at 3, 4, 5, and 6 kilofeet (1 kft; 1 kft = 304.8 m). The straight, thin black lines are the CO–KS, CO–NE, and KS–NE state borders. NWS WSR-88D radars are shown for Denver, CO (KFTG), Pueblo, CO (KPUX), and Goodland, KS (KGLD). All distances are east–west (X) and north–south (Y) from the Goodland radar.

Weather Surveillance Radar-1988 Doppler (WSR-88D) radar (KGLD) comprised the triple-Doppler radar network for STEPS (Table 1). The three radars were arranged in a roughly equilateral triangle with ~60-km baselines providing radar coverage of eastern Colorado, northwestern Kansas, and southwestern Nebraska (Fig. 1). All of these radars measure reflectivity (Z_h) and radial velocity (V_r) derived from transmitted and received signals that are horizontally polarized. The research radars also measure the following polarimetric variables: differential reflectivity (Z_{dr}), linear depolarization ratio (LDR), the correlation coefficient (ρ_{hv}), and the differential propagation phase (ϕ_{dp}). Overviews of polarimetric variables and their use in bulk hydrometeor detection can be found in Herzegh and Jameson (1992), Doviak and Zrnić (1993), Bringi and Chandrasekar (2000), and Straka et al. (2000). Such capabilities provide particle shape and size information, which can be combined with air temperature from a local sounding to infer hydrometeor types within storms (Herzegh and Jameson 1992; Conway and Zrnić 1993; Carey and Rutledge 1996; Carey and Rutledge 1998; Straka et al. 2000; see following section for details).

The CHILL and S-Pol Z_h, Z_{dr}, and LDR fields along with radial velocity data and received powers from each horizontally and vertically polarized channel were routinely interpolated onto a 0.5-km resolution Cartesian grid using NCAR's Sorted Position Radar Interpolator (SPRINT) (Mohr and Vaughn 1979; Miller et al. 1986). Second trip echo contamination in the CHILL data was eliminated by thresholding on differential propagation phase.[2] The S-Pol radial velocities were omitted where sidelobe contamination was suspected. After interpolation, the velocity data were unfolded by means of NCAR's Custom Editing and Display of Reduced In-

---

[2] Data were omitted when $\phi_{dp} > -5°$ prior to 2338 UTC. Past this time differential phase shift values had increased within the first trip echo such that a more conservative threshold of $\phi_{dp} > 30°$ was required.

TABLE 2. Thresholds used to construct membership beta functions in the fuzzy logic hydrometeor classification.

| Type	Z_h (dBZ)	Z_{dr} (dB)	K_{dp} (° km^{-1})	LDR (dB)	ρ_{hv}	T (°C)
Drizzle	<28	0 to 0.7	0 to 0.03	<−32	>0.97	>0
Rain	25 to 60	>0.7	0.03 to 6	−34 to −27	>0.95	>−10
Dry snow	<35	>0	0 to 0.6	<−25	>0.95	<0
Wet snow	<45	0 to 3	0 to 2	−13 to −18	0.82 to 0.95	−1.5 to 2.5
Vertical ice	<35	−0.5 to 0.5	<−0.25	<−24	>0.95	<0
Low-density graupel	40 to 50	−0.5 to 1	−0.5 to 0.5	<−30	>0.96	<−1
High-density graupel	40 to 55	−0.5 to 3	−0.5 to 2	−25 to −20	>0.95	−15 to 15
Small hail (D < 20 mm)	50 to 60	−0.5 to 0.5	−0.5 to 0.5	−18 to −24	0.92 to 0.98	<18
Large hail (D > 20 mm)	>55	<0.5	−0.5 to 1	>−20	0.84 to 0.92	N/A
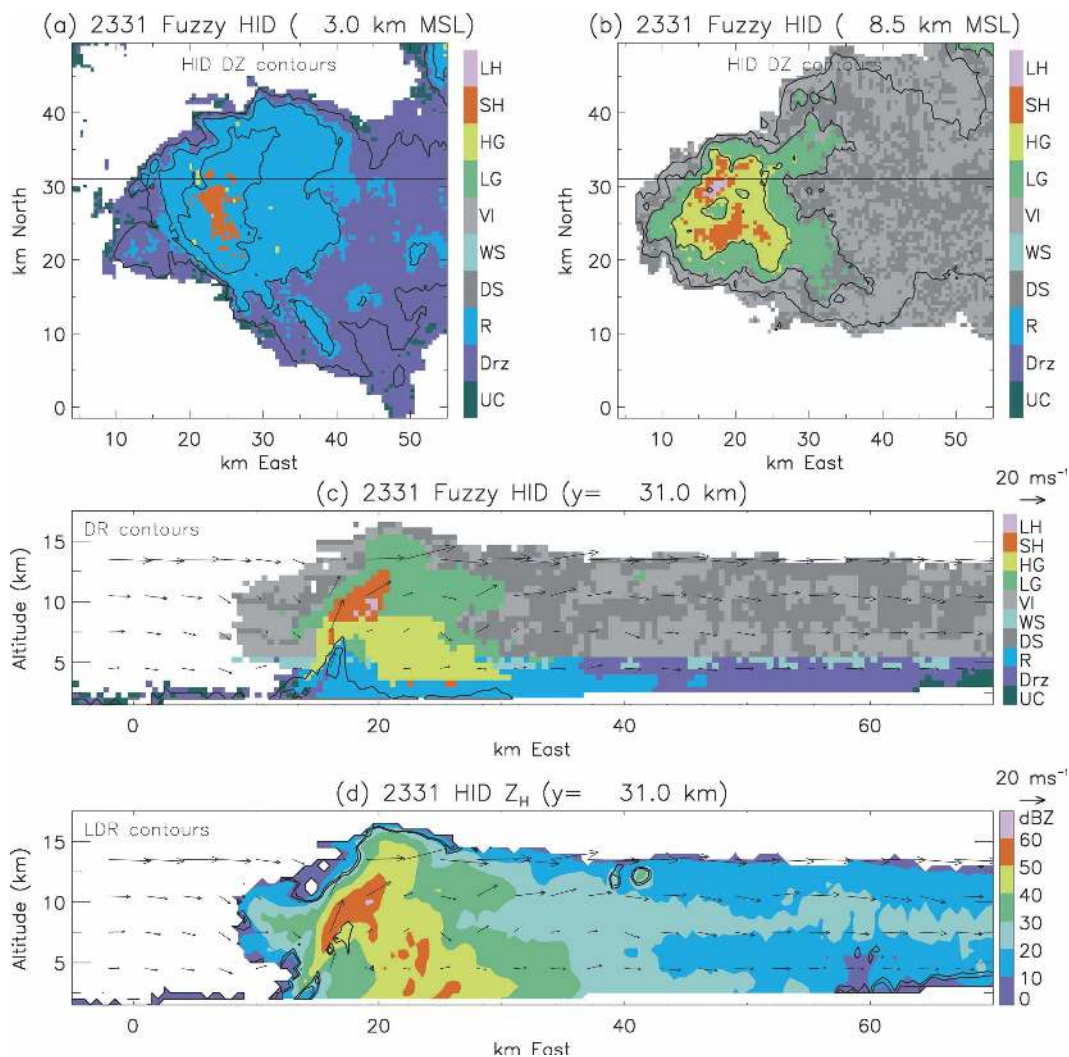
FIG. 2. Horizontal cross sections of FHC output at 2331 for (a) z = 3 km MSL and (b) z = 8.5 km MSL with reflectivity contours overlaid in black starting at 15 dBZ with an interval of 15 dBZ. Vertical cross sections at y = 31 km of (c) FHC with black Z_{dr} contours of 2 and 4 dB overlaid, (d) reflectivity with black LDR contours of −20 and −18 dB overlaid, (e) Z_{dr} color contours, (f) LDR color contours, and (g) K_{dp} color contours. Hydrometeor types are large and small hail (LH and SH), high-density and low-density graupel (HG and LG), vertical ice (VI), wet and dry snow (WS and DS), rain (R), drizzle (Drz), and unclassified category (UC). Storm-relative wind vectors (plotted every 3 km) in the vertical plane are overlaid onto (c)–(g) for reference.

formation in Cartesian Space (CEDRIC) software (Mohr et al. 1986).

The three-dimensional wind fields were computed using the radial velocities from all three radars when available; otherwise, winds were computed from only two radars. Interpolated radial velocities were advected during the synthesis process in accordance with the method outlined by Gal-Chen (1982). Vertical air motion was obtained by integrating the continuity equation using the variational scheme (O'Brien 1970). This synthesis procedure was done approximately every five minutes (synchronized full volumetric scans of the storm were done by all three radars at this time interval) for 36 volume scans during the nearly four-hour observation period 2130 UTC 29 June through 0115 UTC 30 June.

At 0004 UTC 30 June, NSSL launched a balloon that provided vertical profiles of electric field and temperature through the updraft. The temperature sounding

was used in the classification algorithm for hydrometeor types from polarimetric radar data.

b. Hydrometeor classification

The original CHILL and S-Pol polarimetric data were first edited to eliminate noise, clutter, and suspect data using thresholds in ρ_{hv} and the standard deviation of ϕ_{dp}. These methods have been described in Ryzhkov and Zrnić (1998) and used in studies such as Carey and Rutledge (1996, 1998, 2000) and Cifelli et al. (2002). Specific differential phase (K_{dp}) was then calculated from the differential phase in the manner outlined in Hubbert and Bringi (1995) and Carey et al. (2000). These edited data were separately interpolated with SPRINT to the same 0.5-km grid. A fuzzy logic hydrometeor classification algorithm (hereafter FHC), adapted from Liu and Chandrasekar (2000) and Straka et al. (2000), was implemented for the Cartesian gridded data to estimate bulk hydrometeor types within the
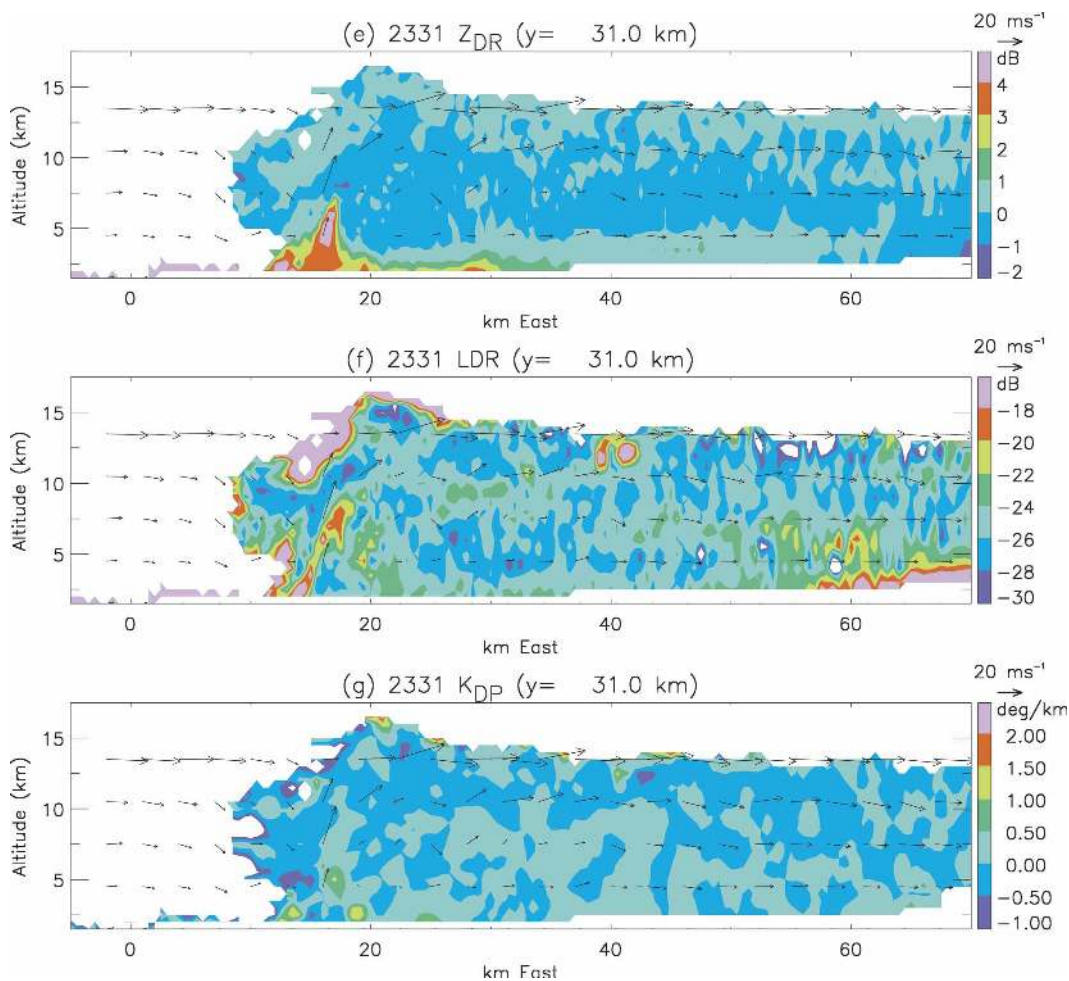

FIG. 2 (*Continued*)

storm (see Table 2 for classification criteria). There are limitations to this procedure that must be kept in mind. Clearly, most radar pulse volumes within a storm consist of more than just one hydrometeor type, thus the FHC-inferred type most likely represents those particles which dominate the radar received signals. FHC-inferred hydrometeor types have been based largely on theory; however, limited studies such as Liu and Chandrasekar (2000) have compared FHC output to some ground-based and in situ observations and successfully validated the FHC procedure in their cases.

An example of the polarimetric data and corresponding FHC results at 2331 during the storm's severe phase are shown in Fig. 2. Horizontal sections in Fig. 2 show that the region of hail is immediately surrounded by rain and drizzle at 3 km (Fig. 2a) and by graupel and ice at 8.5 km (Fig. 2b). The vertical section in Figs. 2c and 2e highlights a so-called Z_{dr} column (Hall et al. 1984; Illingworth et al. 1987), which in this case extends upward to nearly 7 km to temperatures well below freezing. Observed values of Z_{dr} in excess of 4 dB indicate that oblate water drops as large as 4–6 mm (Wakimoto and Bringi 1988; Bringi and Chandrasekar 2000) were present within the west side of the radar echo vault. Elevated K_{dp} values, indicative of high liquid water content associated with the presence of oblate drops (Hubbert et al. 1998), are also seen in the lowest regions of the Z_{dr} column (Fig. 2g). The Doppler-derived winds shown in the vertical cross sections (Figs. 2c–g) indicate that these large water drops were located on the fringe of the updraft and just beneath the so-called embryo curtain (BF76). If the winds allow these sizes of water drops to enter the updraft and rise to freezing levels, they will serve as very efficient cloud water collection centers that can rapidly attain large hailstone sizes.

A small pocket of elevated LDR directly above the apex of the Z_{dr} column is evident in Figs. 2d and 2f. Bringi et al. (1997) showed that an LDR "cap" was consistent with partially frozen rain or wet graupel. Smith et al. (1999) described this feature as raindrops in the process of freezing. The vertical cross section of FHC output in Fig. 2c clearly shows this characteristic signature associated with the process of drops freezing and becoming high-density graupel or small hail. Large values of LDR around the periphery of the storm within low reflectivity are a result of dividing the returned signal in the horizontal channel by the weakly depolarized, nearly noise values in the vertical channel in the LDR calculation and should be considered suspect.

Hydrometeor echo volumes were also calculated for each radar scan time by multiplying the number of grid points (N) that satisfied the hydrometeor type of interest by the volume of a grid box (0.125 km^3).

c. Precipitation growth model

The precipitation growth model is from Knight and Knupp (1986) and, as used here, only includes a high-density growth phase. Since density is used only in the model calculation of particle fall speed, we strongly feel this approach is adequate for our purposes. We will rely on the FHC results to identify the most likely particle types at all times and throughout the observed storm volumes.

The Knight and Knupp growth model uses a simple microphysical scheme whereby all particles are assumed to be spherical and geometrically sweep out cloud water, which is converted to particle mass during each 10-s time step. The amount of cloud water mass that gets converted to particle mass depends on the collection efficiency, which for this study was assumed to be unity. Temperatures and liquid water contents within cloud are based upon their adiabatic values computed from the representative sounding (Fig. 4a) as follows. To simulate horizontal entrainment at each altitude, we linearly decrease the liquid water content from its adiabatic value inside the core updraft with speeds >10 m s^{-1} to 0 at $w \leq 0$ m s^{-1}. The in cloud temperature is treated in a similar way except that it is decreased to the environmental air temperature outside the updraft. In the vertical direction, we further decrease the liquid water content linearly from its adiabatic value at the $-30°$C level to 0 at the $-40°$C level to approximate the effects of glaciation and depletion near storm top. Particles are allowed to grow anywhere between cloud base and the $-40°$C level, though very little increase in mass will occur in the lower regions of the cloud since the cloud liquid water content there is relatively small.

Sensitivity tests conducted by us and by Knight and Knupp (1986) indicate that final particle size depends most on the prescribed cloud liquid water content and the Doppler-derived winds, and less so on the initial locations and sizes of small embryonic particles for the growth trajectories. Further, we agree with Knight and Knupp's (1986) suggestion that adding any further detail or sophistication in the growth model is rather pointless in light of the overwhelming sensitivity to the winds and the cloud liquid water content, which at best, can only be prescribed in some sort of realistic way consistent with our intuition. The model does not consider microphysical processes such as particle freezing, melting, wet and dry growth, shedding of liquid water, or breakup of large water drops. This also means that
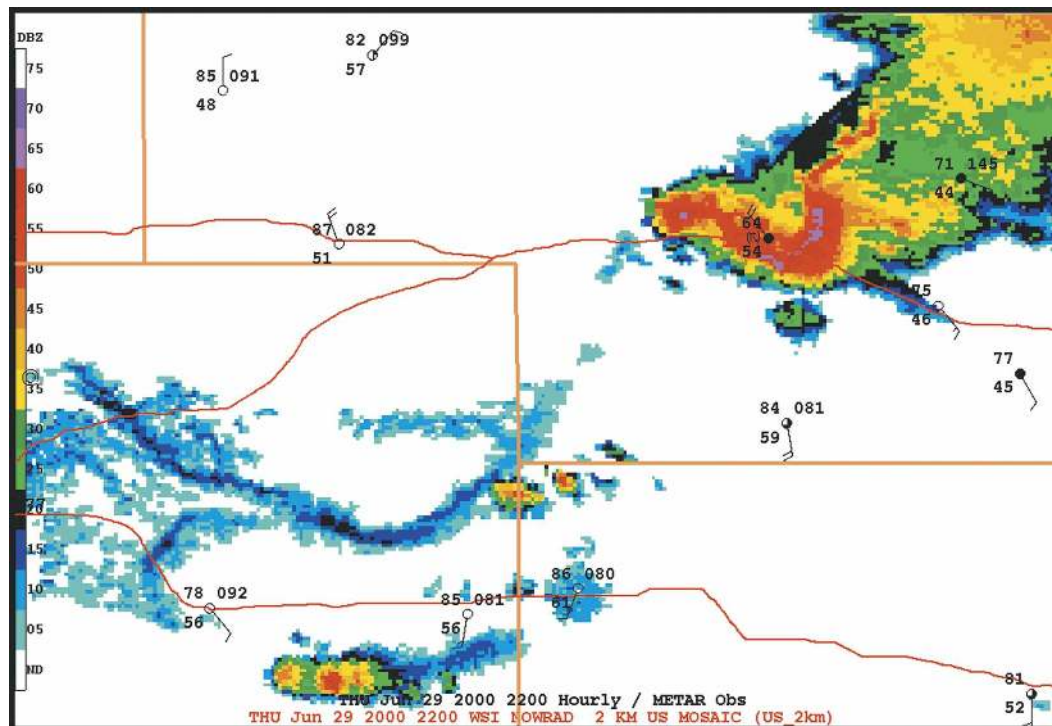
FIG. 3. Subsection of the WSI 2-km national composite of NOWrad reflectivity at 2200 UTC 29 Jun 2000. Surface data are plotted with standard station meteograms: temperature (°F, upper left), dewpoint temperature (°F, lower left), and last three digits of surface pressure (mb ×10, upper right), along with percent cloud cover and weather. Wind speeds are half barb (5 kt) and full barb (10 kt).

whether the particle is liquid or frozen is not an explicit output from the model so that its type must be arbitrarily assigned as a function of size and the temperature at the particle's current location.

It is not our intent in this study to be overly concerned about the details of precipitation growth, but rather to use the growth model as a diagnostic tool to help evaluate possible embryo source regions and growth paths that occur under our prescribed conditions, and to determine how this storm likely became the severe, hail-producing storm that was observed. Results from the precipitation growth model will be combined with all the observations, including results from the hydrometeor classification scheme, to develop a physically consistent picture of the overall microphysical aspects of this storm's evolution.

3. Storm environment and evolution

a. Environmental conditions

Early convection which eventually moved through the STEPS radar domain developed along a southeastward-moving surface boundary (SFB) associated with low-level moisture advection by the southerly flow

ahead of an advancing midlevel short wave that passed over the area (Fig. 3). The SFB was identifiable mostly as a wind shift line with southerly to south-southeasterly surface flow ahead of it and northerly to northwesterly flow behind it. There was about 5°–10°F contrast in dewpoint and very little contrast in temperature across this surface boundary. There was sufficient convergence across the SFB to initiate small cumulus clouds seen as a thin-line echo in the regional composite of WSR-88D data (Fig. 3). Once this SFB entered the northwest corner of Kansas, it could be seen with STEPS radars as a thin-line echo oriented southwest to northeast. The large radar echo mass to the northeast of the SFB also passed southeastward, but it was well outside the STEPS domain. Second trip echoes from this larger mesoscale convective system (MCS) did occasionally contaminate the STEPS radar data.

The environmental soundings (Fig. 4) were taken with NCAR Mobile GPS/Loran Sounding Systems (MGLASS) both ahead of (Fig. 4a) and behind (Fig. 4b) the advancing SFB. High surface-based convective available potential energy (CAPE was 1254 J kg^{-1} according to the 2022 Goodland sounding, Fig. 4a) and a veering, strongly sheared (5–10 m s^{-1} per 3.5 km in the low levels) wind profile are ingredients that favor se-
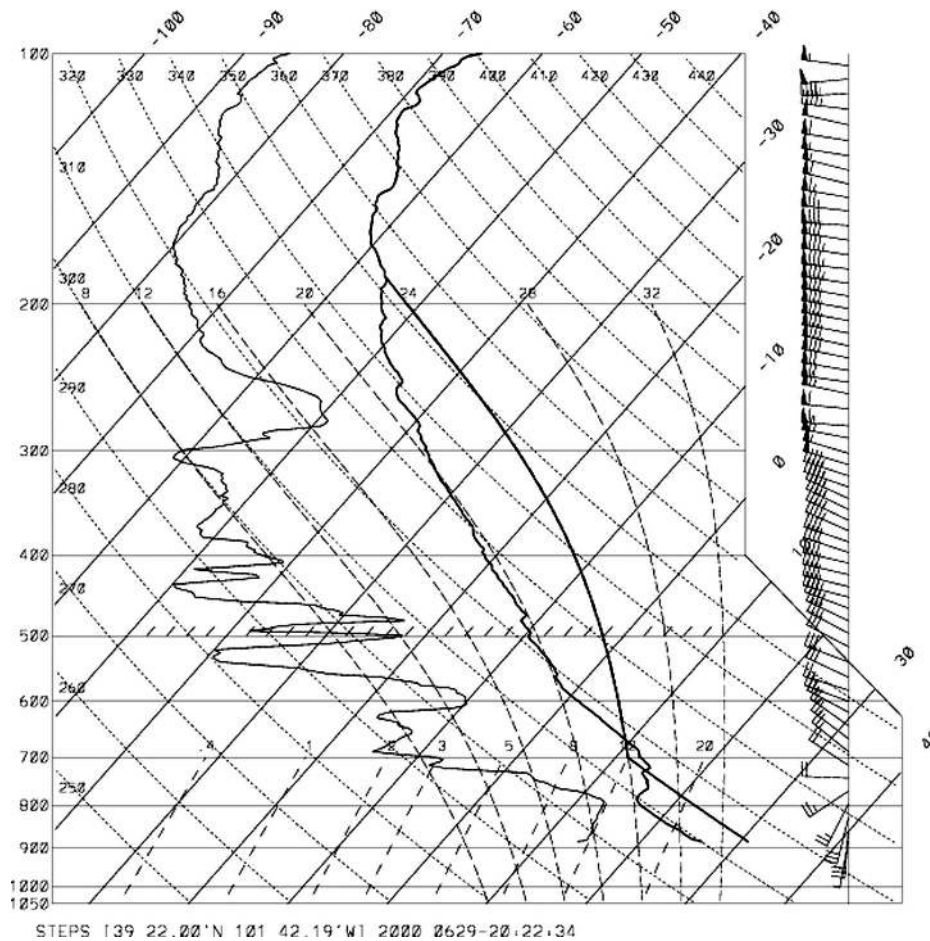
FIG. 4. Skew-T plots of MGLASS soundings on 29 Jun 2000 at (a) 2022 UTC in Goodland and (b) 2338 UTC in northeastern Colorado near Holyoke, north of S-Pol.

vere thunderstorm (supercell) development (Moller et al. 1994). The sounding taken at 2338 (Fig. 4b) behind the SFB showed much drier environmental air above 550 mb ($\sim$5 km). Low-level outflow was not resolved in the Doppler-derived winds since the lowest reliable level was about a kilometer above the surface; however, winds from the NWS operational surface network were consistent with a mid to upper level, rear inflow of northwesterly to westerly air to form the low-level downdraft and outflow, especially during the later intense phase of the storm of interest.

b. Overview of storm evolution

The 29 June supercell (marked as storm A in Fig. 5) was first detected as a small echo at 2130 along the southeastward-moving SFB. Another storm (B in Fig. 5) persisted throughout most of storm A's lifetime, although it did not become severe, unlike storm A. During the period 2130–2325, prior to its right turn and

tornadic stage, storm A moved[3] east-southeastward, toward 115°, at a speed of roughly 10 m s^{-1}. By about 2328 the storm had completed a 35° right turn and began to travel somewhat more slowly with a velocity of 9 m s^{-1} toward 150°. Since the right turn signaled the time when the storm entered its most severe and steady phase, it will be used as a reference throughout the remainder of the discussion.

The rather abrupt looking right turn most evident along the path of the core reflectivity (heavy dark line in Fig. 5a) is actually quite gradual in both updraft and vertical vorticity (Figs. 5b,c). The updraft and reflectivity cores were mostly collocated until the right turn at which time the updraft core became offset toward the right flank (southwest portion of the storm) of the reflectivity core. Likewise, the vorticity core was dis-

---

[3] Storm motion was estimated following the core of reflectivity.

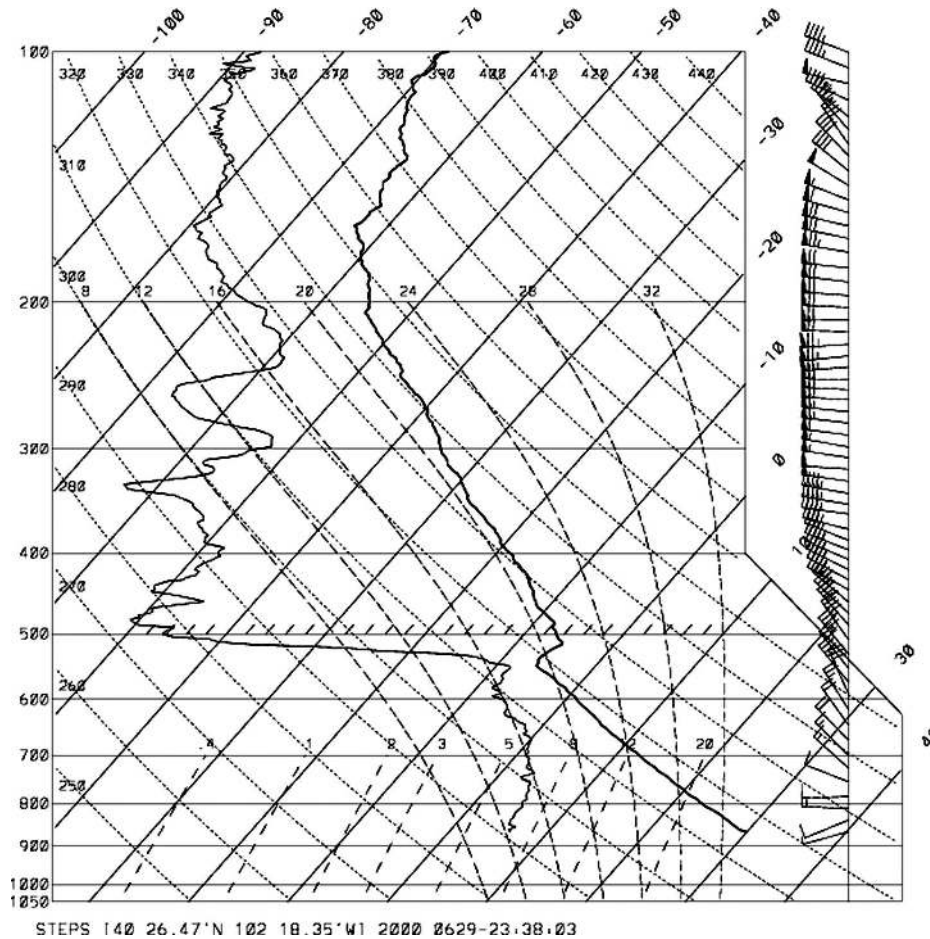STEPS [40 26.47'N 102 18.35'W] 2000 0629·23:38:03

FIG. 4. (*Continued*)

placed farther yet from the right flank of the reflectivity core. This displacement meant that strong cyclonic horizontal flow was now located around the right flank of the updraft. The importance of this development in enabling this storm to produce large hail (>2 cm) will be explored more fully in section 4. Two other noteworthy severe weather events, which occurred when the storm turned right, were the touchdown of a tornado at 2328 (T in Fig. 5) and the dramatic increase in +CG activity. The tornado dissipated around 2344. The NSSL mobile mesonet (Straka et al. 1996) team unofficially categorized the tornado as F1 on the Fujita scale. Only a few positive polarity CG strikes were detected prior to the right turn; however, once the storm had made its right turn, both in-cloud and CG lightning activity increased dramatically, as seen in Fig. 5.

According to *Storm Data* (available online from the National Climatic Data Center at http://www4.ncdc. noaa.gov/cgi-win/wwcgi.dll?wwEvent~Storms), large hail (>2 cm) was first reported at 2235. Hail sizes to 4.5 cm were reported at 2307. By 0054, the storm exhibited large low-level radar reflectivities (up to 75 dBZ) and was still producing very large hail (~5 cm) according to mobile mesonet reports.

c. Detailed storm evolution

Several storm features including volumes of reflectivity, updraft, vertical vorticity, and hail are quantified in Fig. 6. The dashed line shown in Fig. 6a indicates that the total storm volume ($Z_h > 0$ dBZ) gradually increased over the observation period. Since the other radar-derived variables underwent a similar gradual growth trend, we chose to normalize these by dividing them by the total storm volume in order to highlight any shorter-duration surges that might be evident during the storm's evolution. This procedure helped identify four distinct periods in the storm's lifetime: a developing phase (2130–2213), a mature phase (2213–2325), a severe right (SR) mature phase (2325–0036), and a declining phase (0036–0115). These four stages closely follow the life cycle classification scheme for se-
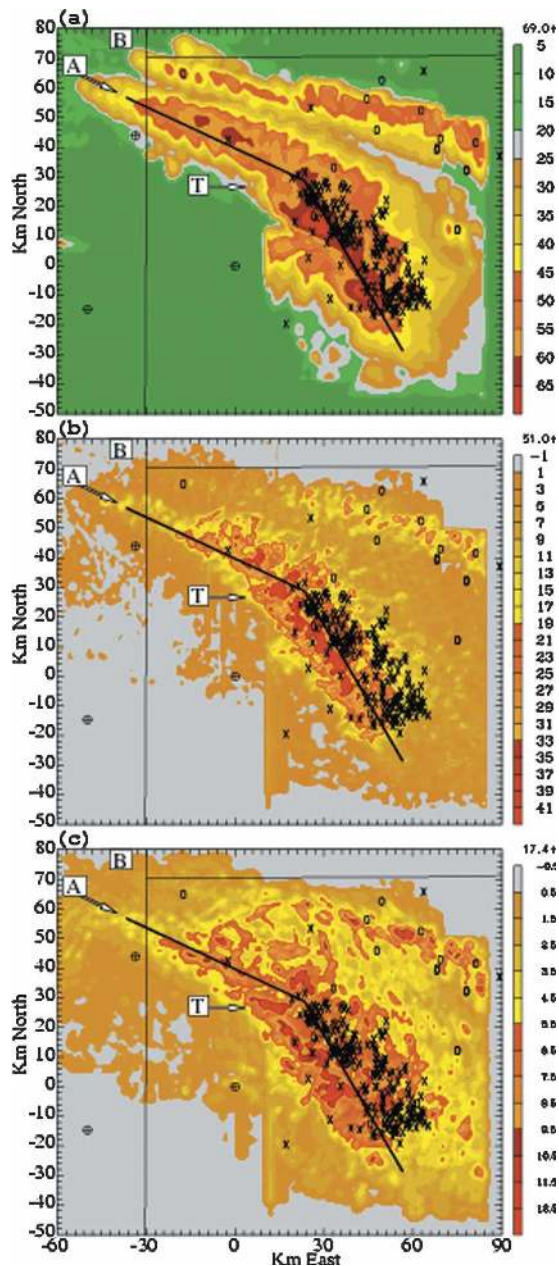
FIG. 5. Swaths of maximum in the vertical column (a) KGLD reflectivity (dBZ), (b) updraft (m s^{-1}), and (c) vertical vorticity (10^{-3} s^{-1}) for the period 2130–0115 UTC with NLDN lightning data overlaid (x = positive CG flash, o = negative CG flash). Radar locations are denoted with a $\oplus$ symbol, with KGLD at (x, y) = (0, 0). The storm motion (based on the path of the reflectivity core) is highlighted with a black line. The symbol (A) denotes the storm of interest, (B) an adjacent nonsevere storm, and (T) the location of the tornado.

vere storm cells proposed by Browning (1964) as distinct from the three-stage classification scheme used by Byers and Braham (1949) to describe the evolution of individual, nonsevere thunderstorm cells.

Detailed horizontal cross sections of low- and midlevel wind and reflectivity features along with vertical cross sections through the storm core are shown in Figs. 7–11. These cross sections were chosen as representative of the various phases in the lifetime of this storm. The following detailed discussion will follow the time history of events as shown in Fig. 6, while referring to these detailed cross sections when needed.

1) DEVELOPING PHASE (2130–2213 UTC)

Reflectivities were below 50 dBZ, updraft volume was small and transient, and there was no mesocyclonic-strength vertical vorticity ($>10^{-2}$ s^{-1}; Moller et al. 1994) or hail echo volume (Fig. 6). Total lightning flash rates (calculated according to the method outlined in Part II) increased to 10–20 flashes min^{-1}, but no CG lightning was detected (Fig. 6e). Reflectivity structure of the storm at this point was fairly nondescript (not shown). Near the end of this stage, a weak and shallow Z_{dr} column was detected, which indicated the presence of large oblate drops entering the updraft. Soon after the first appearance of the Z_{dr} column, hail above the melting level was evident (Fig. 6d). By 2213, the updraft volume exhibited a sharp increase, and reflectivities above 50 dBZ as well as vorticity greater than 10^{-2} s^{-1} were observed. The storm relative flow was from the south-southwest at low levels, while from the northwest aloft. Reflectivities were as high as 65 dBZ and appeared somewhat multicellular with two distinct updraft cores, the stronger of the two reaching 15 m s^{-1} (Fig. 7c). The stronger of these two cells continued development into the mature phase.

2) MATURE PHASE (2213–2325 UTC)

The volume of updraft greater than 10 m s^{-1} remained high, measurable volumes of high reflectivity and vorticity were present, and two periods of hail growth and fallout were detected (Fig. 6).[4] The total lightning flash rates doubled to peak at ~100 min^{-1} at 2239 then decreased back to ~50 min^{-1}. A few CG flashes were detected and the storm exhibited a vaulted structure in reflectivity during the peak of this phase (2239–2252 UTC, see also Fig. 8c). This vault indicates that a strong, broad updraft persisted over a significant depth and prevented hydrometeors from growing along a path from cloud base to radar detectable sizes within its core. A horizontal cross section through the vault at

---

[4] We have used hail echo volume below the melting level as a proxy for hail fallout since the lowest level radar scans were not consistently available throughout the entire analysis period.
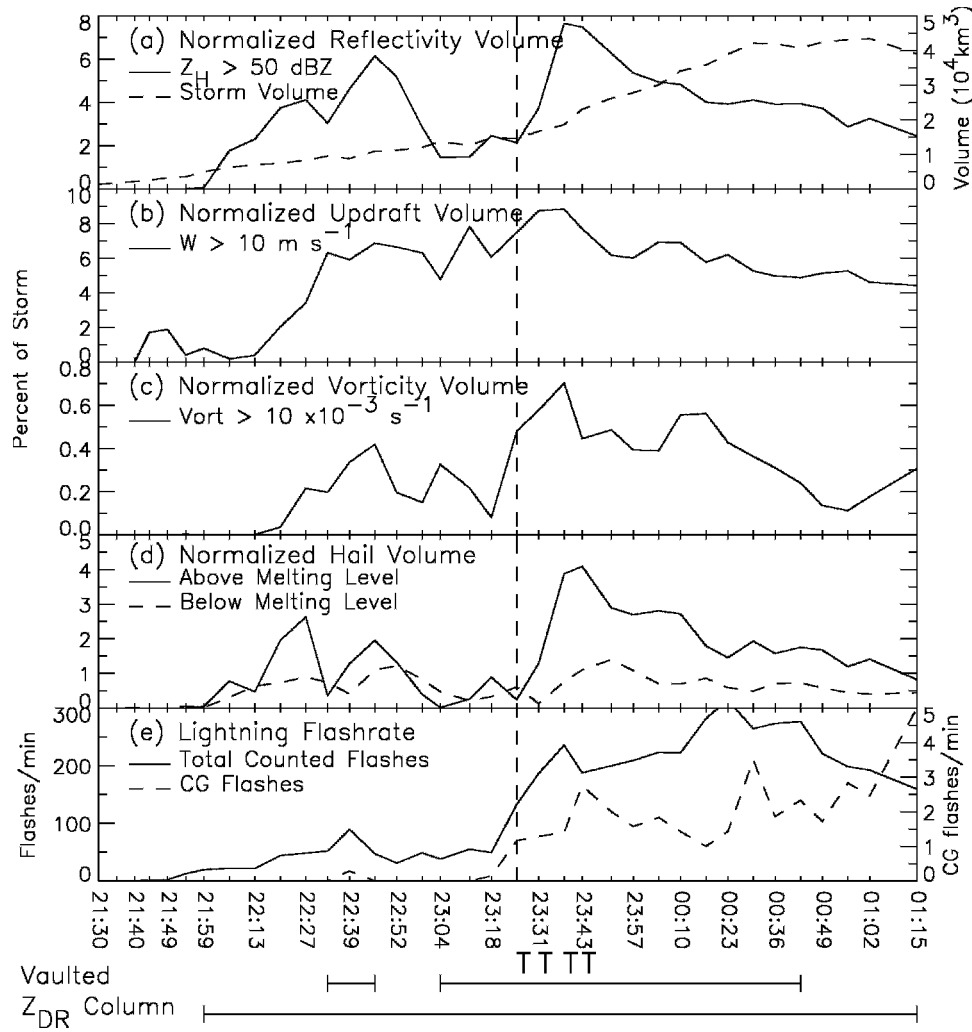
FIG. 6. A time series overview of observed storm characteristics including (a) the total storm volume (km^3) with reflectivity greater than 0 dBZ (dashed line) and the percent of the total storm volume with reflectivity greater than 50 dBZ (solid line), (b) percent of the total storm volume with updrafts greater than 10 m s^{-1}, (c) percent of the total storm volume with vertical vorticity greater than 10^{-2} s^{-1}, (d) percent of total storm volume with hail detected by FHC above the melting level (solid line) and below the melting level (dashed line), and (e) total lightning flash rate (solid line) and cloud-to-ground lightning flash rate (dashed line) for each time (UTC) during the analysis period. The T indicates the tornado was on ground at that time, and bars across the bottom of the plot indicate the times when the storm had a vaulted reflectivity structure or a Z_{dr} column of at least 2 dB in magnitude. The vertical dashed line represents the time that the storm made its right turn.

2239 reveals a bounded weak echo region (BWER[5]) in the reflectivity field with the corresponding updraft core in its center (Fig. 8b). A shallow isolated cell was present to the southwest of the storm at this time (Fig.

[5] In our view, the BWER is an inverted bowl-like structure where the inside surface of the bowl represents the upward displacement, by an intense updraft, of the family of three-dimensional trajectories of significantly sized precipitation particles.

8a), which may have provided some embryos for hail growth as it was upwind of the storm relative low-level inflow. The low-level, storm-relative flow exhibited more cyclonic curvature, while the midlevel flow was more westerly and divergent around the updraft core (Fig. 8). The end of this phase was marked by a brief decline in the high reflectivity, vorticity, and hail volumes (Fig. 6).

We can only speculate about the cause of this decline since there are a number of potential causes, acting
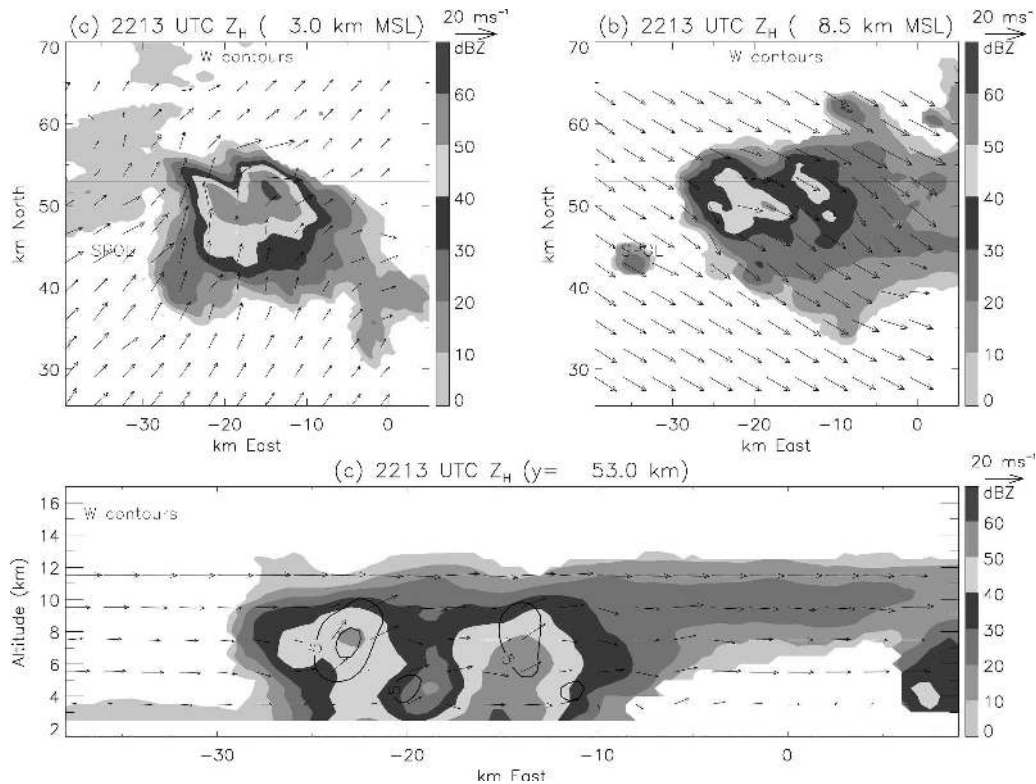
FIG. 7. Winds and storm structure illustrating the temporal boundary between the early developing and ordinary mature phases at 2213 UTC: (a) horizontal cross section of grayscale reflectivity at $z = 3$ km and bold black updraft contours beginning at 5 m s^{-1} with a contour interval of 10 m s^{-1} (due to the weak updrafts at this synthesis time no contours are evident in this frame), (b) horizontal cross section of grayscale reflectivity at $z = 8.5$ km with bold black updraft contours beginning at 15 m s^{-1} with a contour interval of 15 m s^{-1} (again, no contours are evident in this frame due to the weak updrafts at this time), and (c) vertical cross section of grayscale reflectivity at $y = 53$ km with bold black updraft contours beginning at 5 m s^{-1} with a contour interval of 10 m s^{-1}. All plots have storm-relative wind vectors overlaid.

singly or in concert. Most likely, the earliest phases of this storm are best described as consisting of a modest-strength evolutionary component on top of an initially weaker, but steadier (perhaps persistent is a better term) component. The storm transitions from a rapidly evolving, weak phase to a slowly evolving (near steady), strong phase somewhat similar to the separate concepts of steady, and weak and strong evolution presented by Foote and Frank (1983).

3) SEVERE RIGHT MATURE PHASE (2325–0036 UTC)

A dramatic increase in vorticity volume and touch-down of the tornado, as well as the right turn itself, distinguished the beginning of the SR phase at 2325 (Fig. 6). A steady increase in total lightning flash rate and a sudden rise in CG flash rate (predominantly of positive polarity) were also evident (Fig. 6e). The low-level reflectivity field at 2325 exhibited a flanking line

of weak echo extending westward from the high reflectivity core (Fig. 9a). This flanking line was likely associated with outflow[6] beneath one of the early updraft surges that was now dissipating as it continued toward the northeast. The midlevel reflectivities show evidence of two BWERs, one more pronounced within a stronger (up to 45 m s^{-1}) and deeper updraft and located nearer the core of the storm and the other weaker and located more along the flanking line (Fig. 9).

In environments with a clockwise-turning hodograph, Rotunno and Klemp (1982) found that a vertical pressure gradient is enhanced on a storm's right flank, favoring right-flank updraft growth and intensification. Through numerical simulations, Klemp et al. (1981)

---

[6] Our synthesis does not show such a so-called rear flank downdraft, but this is likely due to the lack of low-level radar data needed to detect the associated (and apparently shallow) divergence near the ground.
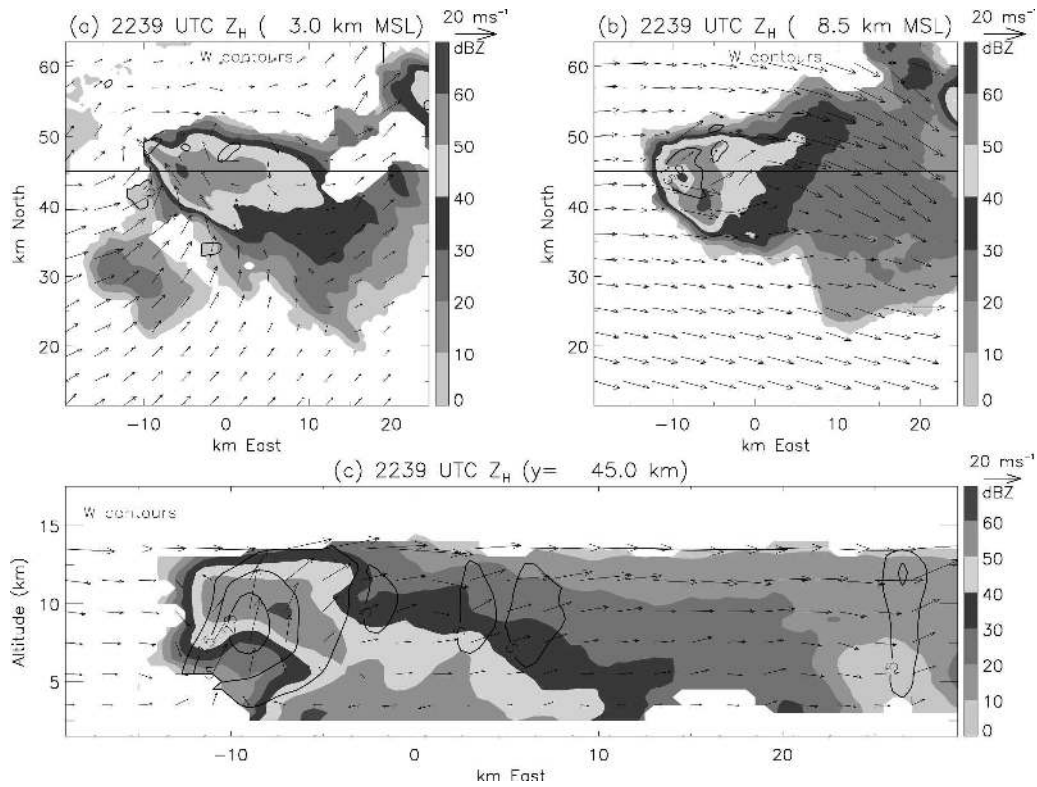
FIG. 8. As in Fig. 7 except for synthesis showing the storm structure during the ordinary mature phase at 2239 UTC and (c) y = 45 km.
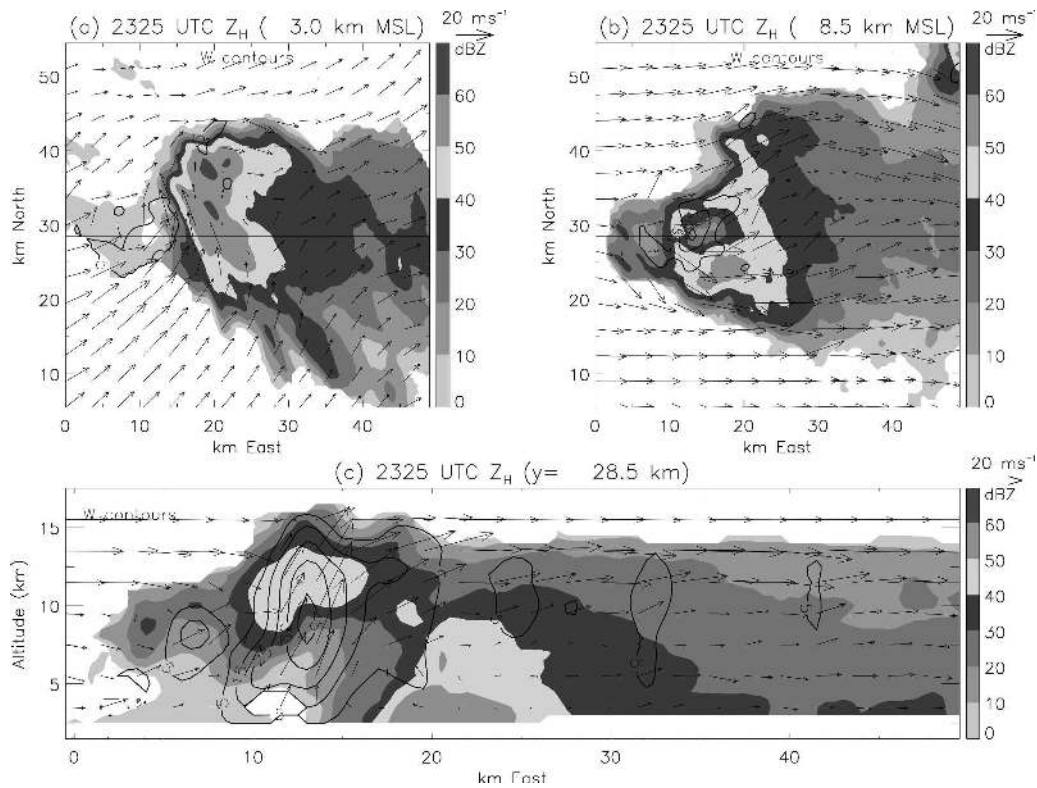

FIG. 9. As in Fig. 7 except for synthesis representing the beginning of the tornadic period within the SR mature phase at 2325 UTC and (c) y = 28.5 km.

showed that a right turn occurred after the original updraft elongated and split or after a second updraft (possibly initiated along an advancing gust front) developed on the right flank of the original one. Consistent with the latter idea, successive syntheses indicated that the new updraft on the right flank of this storm continued to grow and became dominant, while the original updraft was cut off at low levels and then dissipated. There also appears to be more divergence of the storm relative flow around the midlevel updraft at this time, particularly to its south, leading to the reflectivity maximum southeast of the main updraft (Fig. 9b).

Approximately 20 min after the beginning of the SR phase, the volumes of reflectivity greater than 50 dBZ and hail above the melting level abruptly rose to their peak values (Figs. 6a,d). The vertical vorticity volume greater than 10^{-2} s^{-1} had begun to decline by 2343, coincident with the dissipation of the tornado. At this time, a large area of low-level reflectivities exceeded 60 dBZ and the storm had developed a strong, broad updraft on its right flank (Fig. 10). The midlevel BWER seen in Fig. 8 had nearly filled in with high reflectivities by 2343, presumably due to the presence of large hydrometeors. Cyclonic low-level storm relative flow and strong divergence of the midlevel storm relative winds around the main updraft were still apparent. A low-level hook echo, typical of most "classic" supercells, was not detected until near the middle of this phase even though the storm had been a severe right–moving storm for over 30 min. The total lightning flash rate reached its peak value of near 300 flashes min^{-1} near 0020. There was a distinct spike in CG flash rates near the end of this period (Fig. 6e).

4) DECLINING PHASE (0036–0115 UTC)

This phase began near 0036 UTC when the high reflectivity, updraft, vorticity, and hail volumes were waning (Fig. 6) and ended as the storm propagated outside of the radar domain. It should be noted that this storm persisted for another three hours as part of a large mesoscale convective system (MCS to the upper right in Fig. 3) before complete dissipation. At 0036, the broad area of low-level reflectivity greater than 60 dBZ had elongated parallel to the storm relative flow and a midlevel BWER could be discerned again (Fig. 11). A new cell had developed to the northwest of the storm near 0004 and can be seen in Fig. 11a. The low-level storm relative flow was still slightly cyclonic along the storm's right flank, and midlevel divergence around the updraft was still evident (Fig. 11). Even in the presence of a strong and broad updraft, the vaulted nature of the storm was beginning to subside, and was gone by 0049.

The absolute peak in the CG flash rate occurred just at the end of the analysis period (Fig. 6e).

4. Airflow and hail growth

a. Overview of airflow and radar echo structure

There are several features evident in the time–height contour plots of stormwide maximum values and volumes associated with the updraft and vertical vorticity (Fig. 12) that are likely strong controls on the production of graupel and hail (Fig. 13). As seen in Fig. 12a, there are six distinct surges in updraft intensity that exceed 30–50 m s^{-1} and last for about 10–30 min. The last surge after 2357 and lasting some 40 min occurred during the "most steady" phase of the storm, so we are counting it as only one surge even though there are two somewhat minor surges within it. The updraft intensity (maximum values in Fig. 12a) and volume (Fig. 12b) were located mostly at or above the 9-km level where the adiabatic liquid water content reached its maximum value, a region where hail should grow most rapidly but not necessarily reach its maximum size. The low- to midlevel right-flank cyclonic flow is evident in both the vorticity maxima (Fig. 12c) and in the volume of vorticity exceeding 10^{-2} s^{-1} after 2325 (Fig. 12d). The very earliest organizing phase of the storm is also evident in the low values of updraft and vorticity prior to about 2213.

In response to storm intensification as revealed in both the updraft and vorticity, reflectivity maxima (Fig. 13a) and volume (Fig. 13b) both increased while the storm echo top steadily rose. The graupel (total of low-density and high-density categories, Fig. 13c) and hail (total of small and large categories, Fig. 13d) volumes deduced with the FHC algorithm show a similar behavior. It is noteworthy that increases in reflectivity volume (Fig. 13b) clearly follow the updraft surges. Since reflectivity must exceed 50 dBZ in the FHC algorithm for hail, the deduced hail echo volumes will also follow the updraft surges. Graupel production (Fig. 13c) also follows these trends.

b. Hail growth calculations

Particle growth calculations were made for ten sizes of starting embryonic particles (0.02, 0.05, 0.1, 0.2, 0.3, 0.4, 0.5, 0.6, 0.8, and 1.0 mm) spaced 1 km apart on a regular 80 km × 80 km horizontal grid, and with starting altitudes every 1 km from 4 to 12 km, for each of 31 synthesis times from 2130 UTC 29 June through 0036 UTC 30 June. Embryos were allowed to grow only from starting locations within the regular grid where there was some radar echo ($Z_h > 0$ dBZ). Such an ensemble
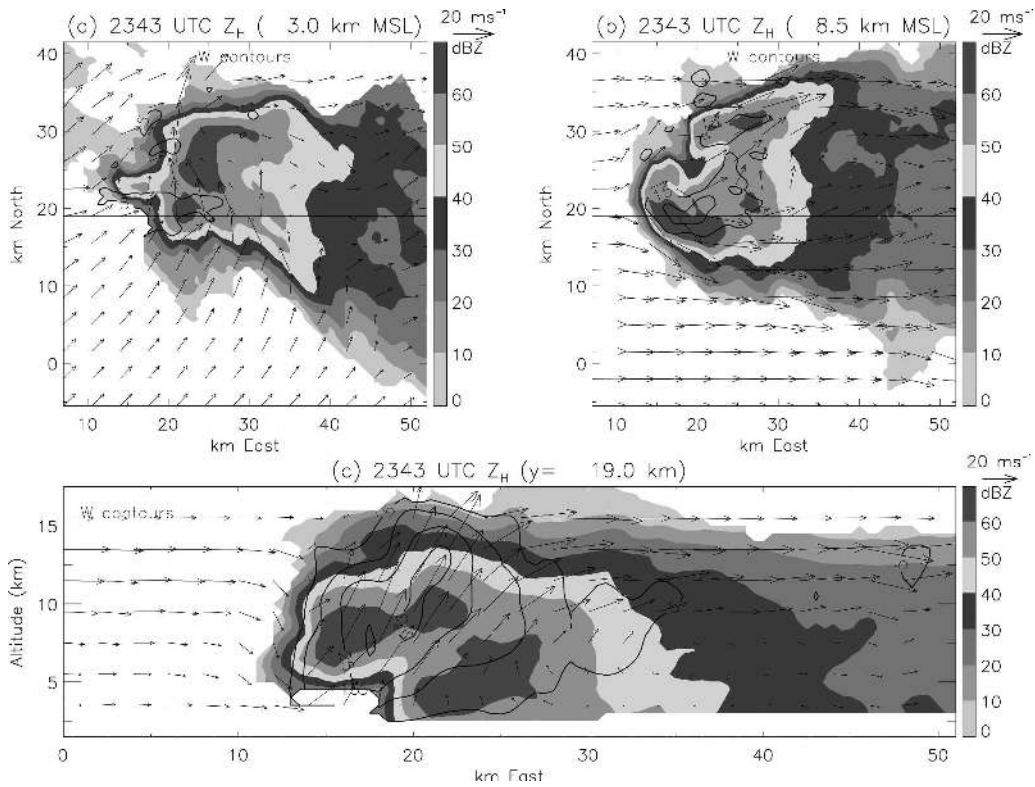
FIG. 10. As in Fig. 7 except for synthesis illustrating the end of the tornadic period within the SR mature phase at 2343 UTC and (c) $y = 19$ km.
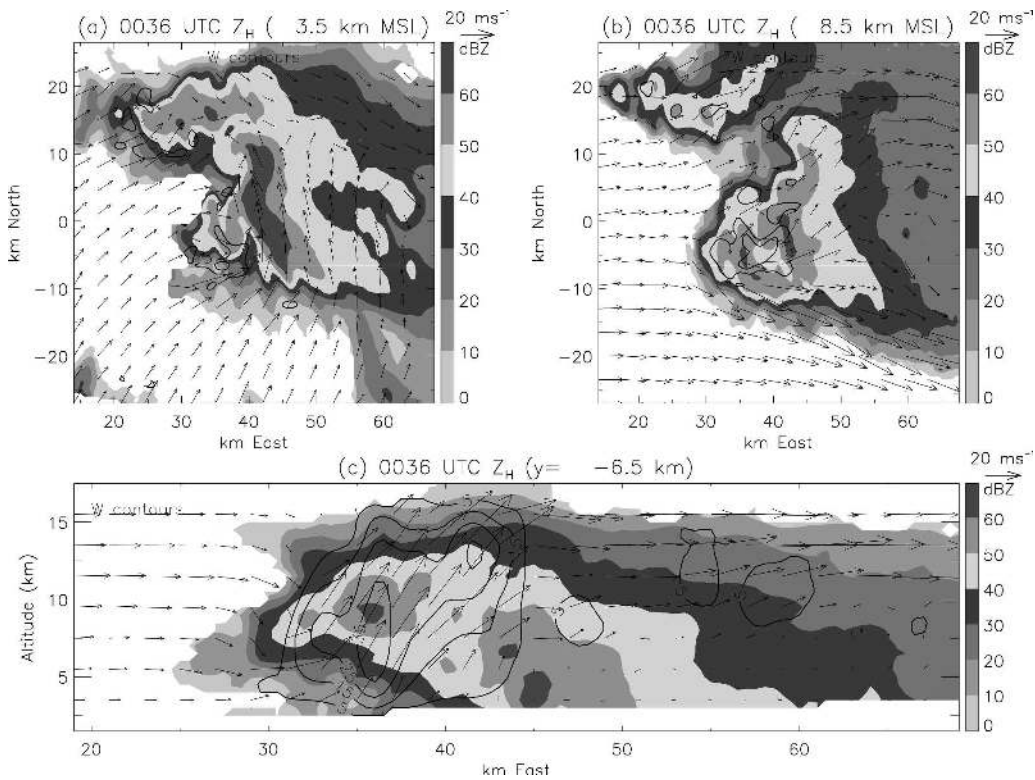

FIG. 11. As in Fig. 7 except for synthesis representing the storm structure in the declining phase at 0036 UTC and (a) $z = 3.5$ km and (c) $y = -6.5$ km.
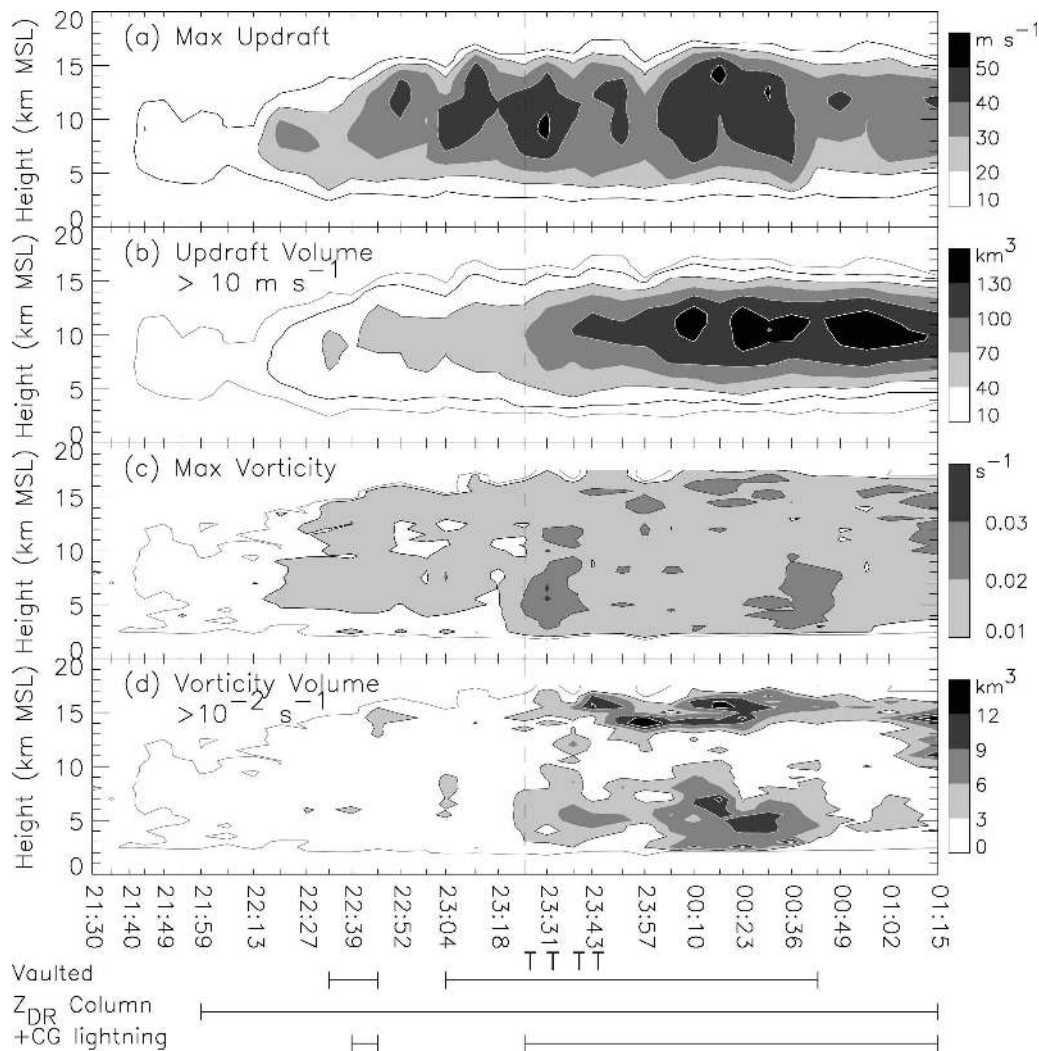
FIG. 12. Time–height contours of (a) maximum updraft (m s^{-1}), (b) updraft volume (km^3) greater than 10 m s^{-1}, (c) maximum vertical vorticity (s^{-1}), and (d) vertical vorticity volume (km^3) greater than 10^{-2} s^{-1}. A thick black line indicating the 10 m s^{-1} maximum updraft contour is overlaid in (b), and the 5×10^{-3} s^{-1} maximum vertical vorticity contour is overlaid in (c) and (d) for reference. The T indicates that the tornado was on ground at that time, and bars across the bottom of the plot indicate the times when the storm had a vaulted reflectivity structure, a Z_{dr} column of at least 2 dB in magnitude, and positive cloud-to-ground lightning. The vertical dashed line represents the time when the storm made its right turn.

of particles was inserted into the flow at each of the 31 synthesis times and allowed to grow over the next 35–40 min using winds from the initial and subsequent seven synthesis times. Winds used were ground relative so that results to be presented represent time-resolved, ground-relative growth trajectories. The total mass of cloud liquid water swept out by each growing particle was determined at the end of each 10-s time step and incorporated into an ever-increasing particle mass and diameter. Each particle was then advanced with winds interpolated to its current location and time after initialization along with a new fall speed calculated from

the new diameter. This procedure continued along each trajectory until the growing particle either fell out (defined as reaching 3 km or lower in altitude) with at least a 2-mm diameter or reached the edge of the computation domain. The results, therefore, also include precipitation particles that are smaller than hail (arbitrarily defined as any particle size ≥10 mm). Since melting with possible shedding of this meltwater are not accounted for in this simple growth model, particles that descend below the melting level (~5 km) cannot lose any mass.
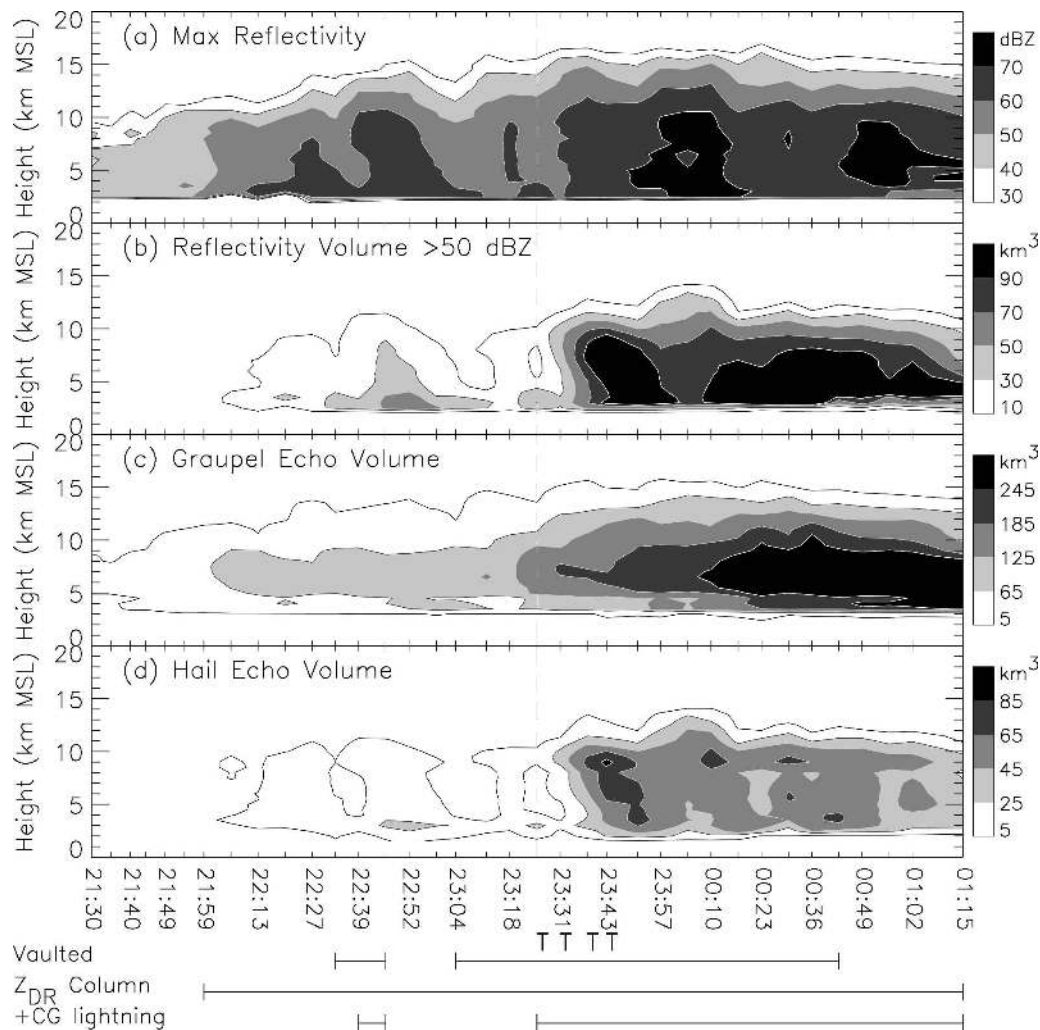
We have somewhat arbitrarily separated calculated

FIG. 13. As in Fig. 12 except (a) maximum reflectivity (dBZ), (b) reflectivity volume (km^3) greater than 50 dBZ, (c) FHC total graupel (low density + high density) echo volume (km^3), with contours beginning at 5 km^3 with a contour interval of 60 km^3, and (d) FHC total hail (small + large) echo volume (km^3), with contours beginning at 5 km^3 and a contour interval of 20 km^3.

precipitation sizes that reach the ground into graupel (diameter <10 mm, the smaller of which will likely completely melt) and hail (diameter ≥10 mm) categories to be consistent with those defined in the FHC algorithm (Fig. 14). The overall trends in calculated graupel and hail growth are shown in Fig. 15 as time–height contour plots of the numbers of trajectory model grid points that satisfied the given size threshold at each height and time within 1-km grid boxes for the entire period when synthesized Doppler winds were available. These plots have been constructed in this way so that we can compare calculated growth with observed growth (Fig. 14). This approach also reveals how the calculated growth responded to the evolution of the storm's kinematic structure.

Both high-density and low-density graupel categories deduced with the FHC algorithm have been summed for presentation in Fig. 14a. Likewise, small and large hail have been summed and shown in Fig. 14b. These plots are similar to Figs. 13c,d, but now include melting to rain and drizzle and stormwide trends in the growth model results for comparison. Based on the melting model presented in Pruppacher and Klett (1997), high-density graupel and small hailstones would completely melt after falling about 1.5 km below 0°C (5 km). No graupel will survive past a 2-km descent, which corresponds to a temperature of about 15°C. Ice particles smaller than 10 mm will completely melt within about a 2.5-km descent, which in this storm corresponds to a temperature of 18°C. The FHC algorithm places more
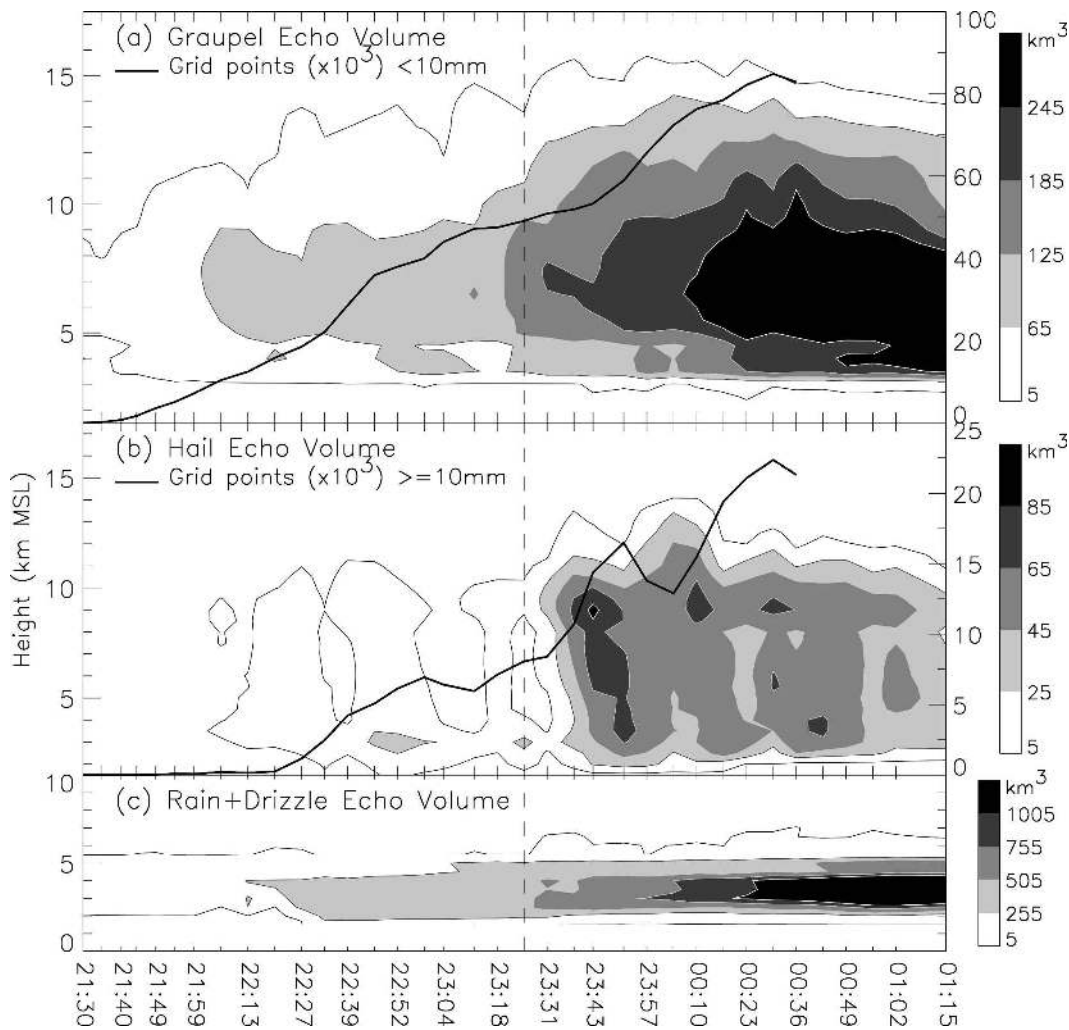
FIG. 14. Time–height contours of (a) FHC total graupel (low density + high density) echo volume (km^3), contours beginning at 5 km^3 with a contour interval of 60 km^3; (b) FHC total hail (small + large) echo volume (km^3), contours beginning at 5 km^3 with a contour interval of 20 km^3; and (c) FHC rain and drizzle echo volume (km^3), contours beginning at 5 km^3 with a contour interval of 250 km^3. Height (km MSL) is denoted on the left axis in (a)–(c). A thick black line indicating the total number of graupel-producing (<10 mm) grid points ($\times 10^3$; see right axis) from the particle growth model at each time is overlaid onto (a), and a similar line indicating the number of hail-producing ($\geq$10 mm) grid points ($\times 10^3$; see right axis) is overlaid onto (b). The particle growth model used Doppler-derived wind data until 0036 UTC.

and more of the graupel and small hail categories into the rain category as precipitation descends, which can be seen in Fig. 14c. The drizzle that is included here comes mostly from the melting of small graupel and other ice particles outside the most active updraft region of the storm.

Results from the precipitation growth model are shown in Fig. 15. It is abundantly clear from these plots that the resolved Doppler wind fields were unable to produce even graupel-sized particles until after about 2148, ~18 min after initial radar detection of the storm. Further, no hail was produced until almost an hour

(2227) after the storm was first detected. There are also obvious surges in the amounts of graupel and hail as demonstrated by the local maxima in the lower half of the storm, below about −10°C. These surges from the growth model correspond quite well with those deduced from the FHC algorithm (Fig. 14).

Fallout locations for hail larger than 30 mm from the growth model were mostly confined to the area of radar reflectivity exceeding 55 dBZ (Fig. 16a). Virtually all of the modeled hail larger than 20 mm fell out along the left flank of the core updraft (Fig. 16b), especially just before the obvious right turn of the storm at 2325.
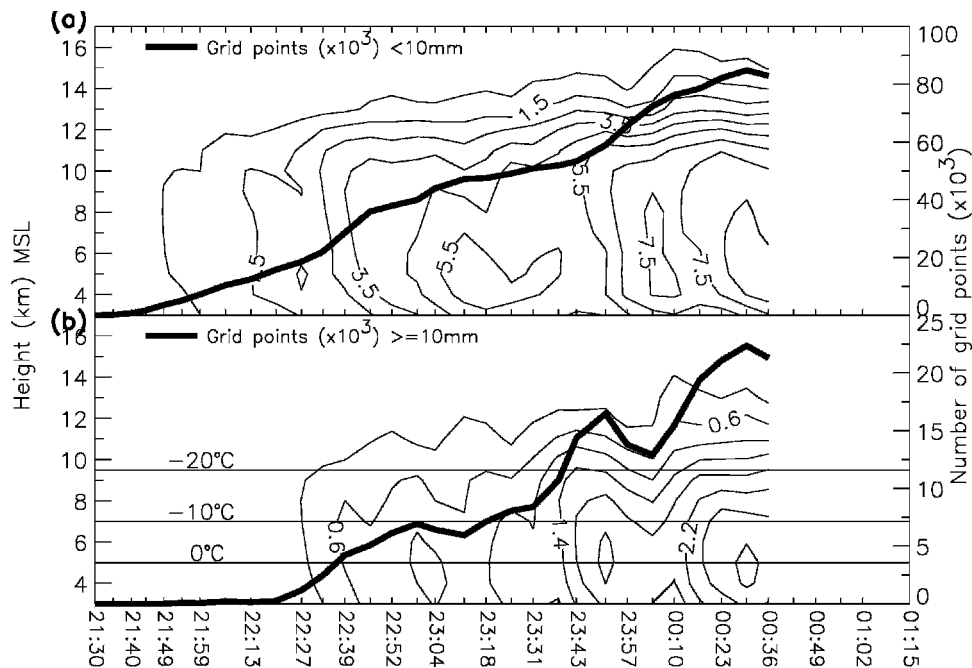
FIG. 15. Time–height contours of the gridded particle growth model output to compare with Fig. 14. Contours represent (a) the number of graupel-producing (<10 mm) grid points and (b) the number of hail-producing (≥10 mm) grid points at each time and height. Contours in (a) begin at 0.5×10^3 and have a contour interval of 1.0×10^3, and in (b) they begin at 0.2×10^3 and have a contour interval of 0.4×10^3. The thick black lines overlaid are as those in Figs. 14a,b. Isotherms are overlaid in (b) to highlight the $0°$, $-10°$, and $-20°$C levels.

Small embryonic particles that eventually fall out as hail originate mostly within the region surrounding the upstream and right flanks of the updraft (Fig. 17). This broad embryo source region (corresponding roughly to the embryo curtain of BF76) extends downward from the mid- to upper-level stagnation zone associated with obstacle flow and around the right flank of the updraft core. The base of the embryo source region in the low levels near cloud base is directly above the broad low-level inflow to the updraft. Since this "embryo corridor" (Nelson 1983) contains either weak updraft or downdraft, most starting particles are able to descend to heights below the level of nondivergence of the updraft. As particles descend, the horizontally convergent flow in the lower part of the storm sweeps them toward the updraft core. Foote (1984) pointed to this horizontally convergent flow as the fundamental way by which updrafts can ingest small embryonic particles for growth to hail sizes.

There are essentially two growth paths that intermingle within the updraft core, one from the low-level inflow (Fig. 17, INFLOW) and one from the upwind stagnation zone (Fig. 18). The inflow path marked in Fig. 17 represents growth from scratch of small cloud droplets (~20–50 μm). These growing particles will ar-

rive in the midlevels and generally be smaller than ones (~millimeter sizes) sedimenting around the right flank of the updraft from midlevels (Fig. 18, RF) as they move cyclonically into the updraft core. Particles along this path will tend to be larger than ones from the low-level inflow when the two growth paths cross.

Once growing particles pass through the updraft core, size-sorting along the anticyclonic path toward the left flank of the storm will occur, with larger particles descending first as they pass out of the core updraft and smaller particles staying in the S-shaped path (shown most clearly in Fig. 17) until they move farther to the right at which time they fall out. Early in the storm's evolution, when the vorticity was weaker and more confined on the right flank of the updraft maximum, these two colliding paths were much less pronounced. With time, the area and strength of right-flank cyclonic vorticity increased leading to more of the types of trajectories illustrated in Figs. 17 and 18, with bigger particles now tending to originate more toward the right flank and smaller particles <10 mm continuing to originate along the inflow path and moving into the anticyclonic path aloft.

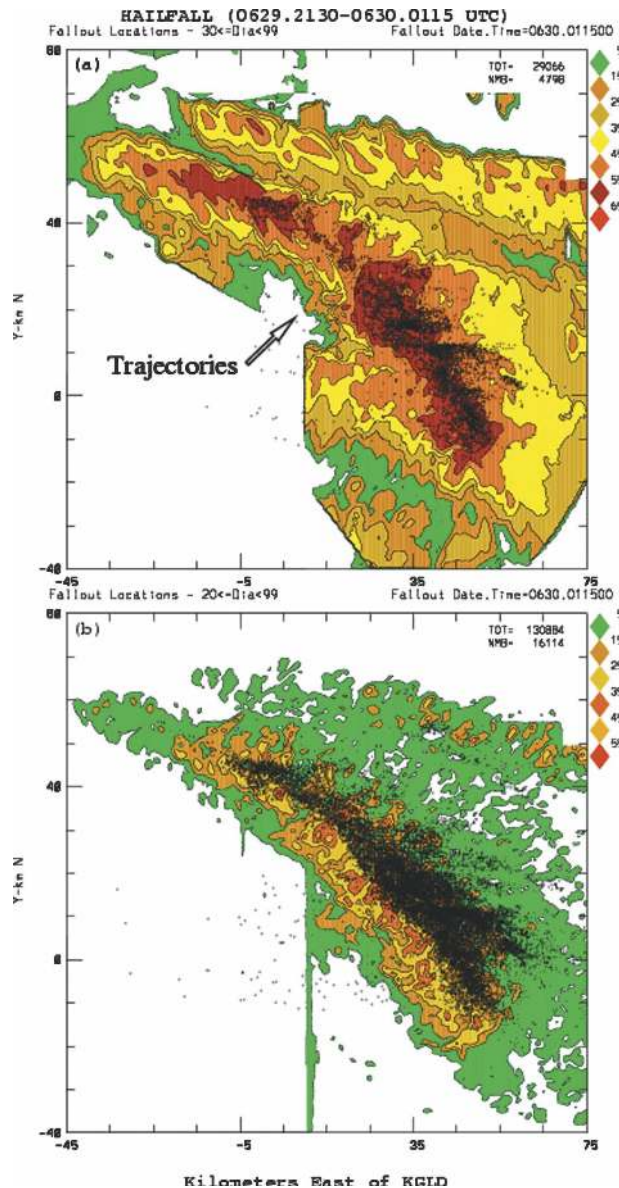To find out how critical the sizes and magnitudes of updraft and vorticity were to the production of hail, we

FIG. 16. Swaths of maximum in the vertical column (a) KGLD reflectivity (dBZ) and (b) updraft (m s^{-1}) for the period 2130–0115 UTC with particle growth model hailfall overlaid as black dots. Modeled hailfall with sizes greater than 30 mm (rather than 20 mm to reduce the number of fallout points so that the underlying reflectivity structure is visible) are overlaid in (a) and greater than 20 mm in (b). The trajectories shown in Figs. 17 and 18 are from the area highlighted in (a).

FIG. 17. Representative hail growth trajectories from embryonic particles (20-μm diameter) started at 2.5 km near cloud base. Trajectories leading to hail (diameter $\geq$10 mm) that falls out below 2 km are overlaid onto (a) horizontal ($z = 2.5$ km) and (b) vertical ($y = 32.5$ km) sections of vertical air motion. The grayscale contours of vertical motion are 2, 12, and 22 m s^{-1}. The black contour line represents -10 dBZ.

performed precipitation growth calculations assuming that each of the wind synthesis times represented a steady kinematic structure. This simplification was done so that results from precipitation growth could be more easily compared to the evolution of the synthesized winds. Histories of the percents of storm volume occupied by strong updraft ($>$10 m s^{-1}) and mesocy-
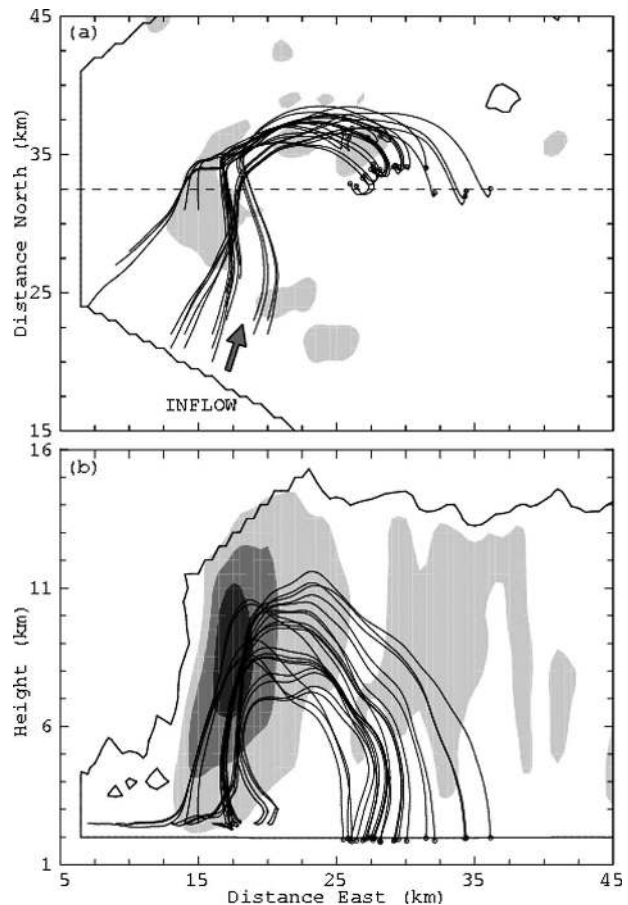
clonic-strength vertical vorticity ($>$10^{-2} s^{-1}) are compared with the resulting precipitation particle sizes from the growth model in Fig. 19.

It is quite clear from this analysis that hail larger than 10 mm can be grown in direct response to increases in updraft volume as seen at 2149 and 2159 (Fig. 19). However, these two small surges along with some of the other fluctuations seen in Fig. 19 should be considered as relatively minor when compared to the much more obvious increase following 2227. Continued increases in updraft volume after 2213 result in continued increases in the number of favorable trajectories leading to hail larger than 10 mm. However, it is noteworthy that hail larger than 20 mm also requires an increase in the volume of mesocyclonic-strength vorticity within the storm, as seen by the increase in percent of favorable trajectories for this final size only after 2220. Cycloni-
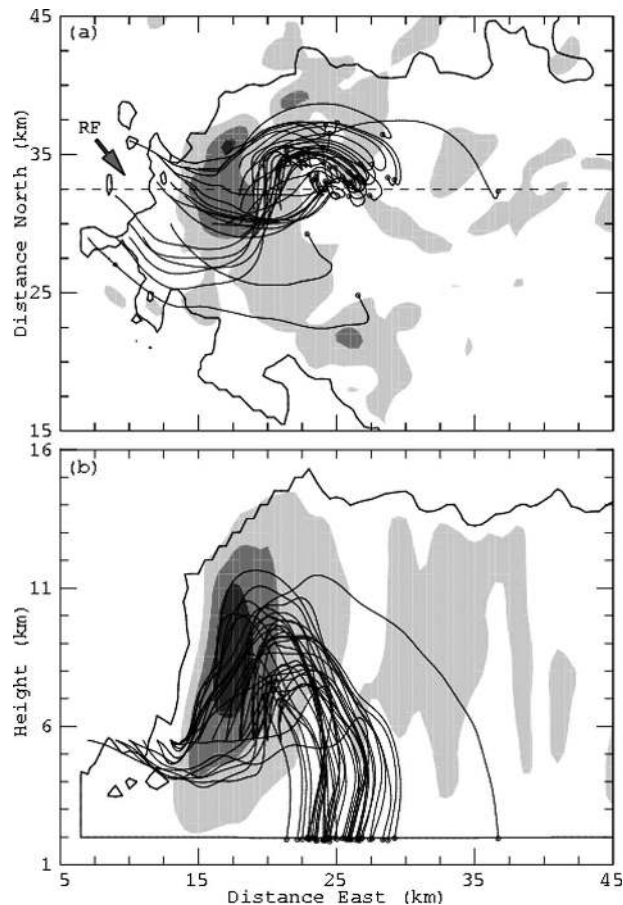
FIG. 18. As in Fig. 17 except for (a) horizontal (z = 5.5 km) section and embryonic particles (100-μm diameter) started at 5.5 km.

cally curved flow in the low- to midlevels was found to be important in recycling sub- to near-millimeter particles from the upwind stagnation zone into the updraft for continued growth to hail sizes (see Fig. 17). If the updraft is bigger, more of these recycling trajectories are favored to produce large hail. It is also evident in Fig. 19 that hail is grown at the expense of graupel as shown by the decline in trajectories favoring graupel after 2227.

5. Summary

This well-observed severe storm has given us the opportunity to study in some detail the kinematic and microphysical evolution from its earliest developing phase through its mature and dissipating phases. The developing phase was important not only in organizing the storm upscale from its initial multicellular structure to one more commonly associated with steady, intense supercells but also in allowing enough time for the

storm to produce an ample supply of embryonic particles for future graupel and hail production. The storm slowly grew in size and intensity until large areas of strong updraft ($>$10 m s^{-1}) and mesocyclonic-strength vorticity were present. This supercellular structure with strong cyclonically curving flow in the low- to midlevels around the right flank of the updraft core made it possible for graupel and hail to be readily grown through a recycling of particles which had initially grown to near-millimeter sizes in their first pass through the updraft. Polarimetric radar observations indicated the presence of liquid water drops as large as 6 mm entering the updraft in locations where they could easily grow into large hail. Elevated LDR caps on top of the Z_{dr} columns further support the notion of large drops being carried aloft and freezing.

Several surges in the updraft were observed to be superimposed upon the more steady, broadscale flow field associated with the SR mature (Browning 1964), or supercellular, phase. These surges persisted for the 20-min periods typical of smaller convective cells such as described by Byers and Braham (1949). Twenty minutes is about how long it takes for a convective bubble to rise to its level of neutral buoyancy and the precipitation produced along the way to fall out. Each of these updraft surges was accompanied by surges in the observed reflectivity (graupel and hail) as well as lightning activity, particularly +CG strikes. We can only speculate on the likely causes of these updraft surges. The reflectivity surges led to increased rainout into intruding midlevel air, which in turn could modulate low-level cold pool production and outflow. These modulations, if present, could then feedback on the amount of low-level convergence along the leading edge of the expanding outflow, and thus modulate the updraft. It is extremely difficult to observe this kind of feedback, so its exact details can only be revealed with fully four-dimensional, high-resolution numerical models.

The exact processes that lead to near-millimeter to millimeter-sized embryonic particles large enough to grow to hail cannot be accurately diagnosed with the resolved Doppler winds. Therefore, it has been customary in studies of hail growth (e.g., Nelson 1983; Foote 1984) to assume that near-millimeter to millimeter-sized embryos exist throughout the storm volume and then to determine where in the storm these particles are most likely to continue growing to hail sizes.

We found that, if near-millimeter to millimeter-sized embryonic particles find their way into the updraft, their growth rates are usually fast enough that they can achieve hail sizes and fallout before passing through the layer of high cloud liquid water. However, even if very small (tens of micron diameters) particles somehow got
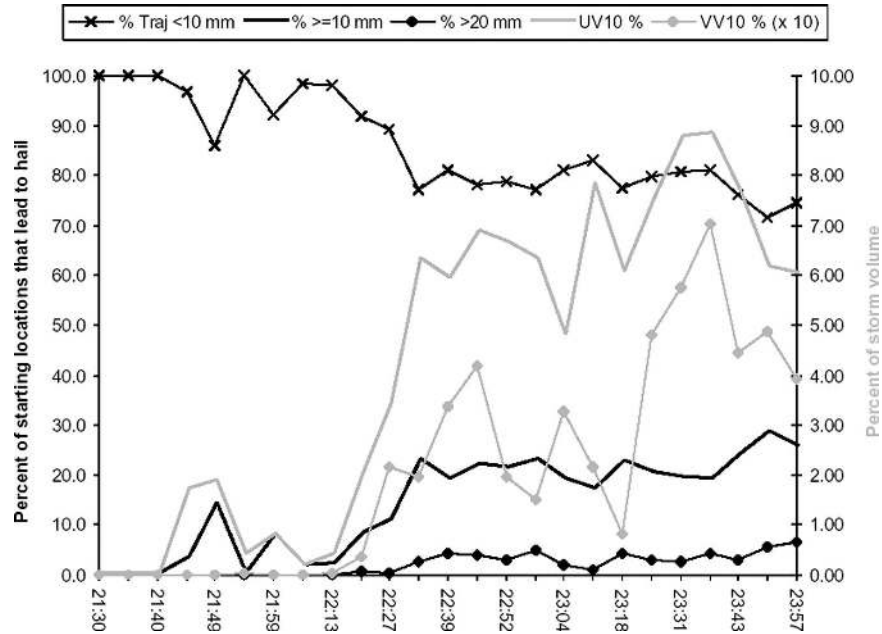
FIG. 19. Time series summarizing normalized updraft >10 m s^{-1} volume (UV10), and normalized vertical vorticity $>10 \times 10^{-3}$ s^{-1} volume (VV10, multiplied by factor of 10 for graphical purposes) in gray on the right axis, and the percent of starting trajectories in the particle growth model that grew to diameters <10, ≥10, and >20 mm in black on the left axis.

into the main updraft, they experienced rather slow growth rates because they tend not to sweep out and collect much cloud water because of their relatively small cross-sectional areas. When the updraft was fairly intense, $\gtrsim10$ m s^{-1}, these small particles were carried upward so fast that they did not have enough time to grow to hail sizes and were simply exhausted into the anvil.

One of the most important aspects of the flow in this storm for the production of large hail was the presence of cyclonic flow in low- to midlevels and on the right flank of the updraft. It appears that this horizontal flow was very efficient in bringing embryonic particles into the main updraft for continued growth. However, there must be sufficient curvature in the flow so that particles are swept into the updraft before they are carried too far downstream from the updraft core.

Most of the air that entered the main updraft core from low levels experienced rapid ascent and was exhausted into the anvil at and above about 13 km. Some updraft air was detrained in midlevels into the downstream region of weaker reflectivities east of the core. Also there were some small areas of downdraft in the low levels on the west side of the core, but there was no midlevel inflow of environmental air into any sort of well-organized downdraft. Cyclonic flow around the storm's right flank in the lowest levels carried air from

the low level region of weak echo into the main inflow path. At higher levels this cyclonic flow carried air directly into the updraft core. Environmental air also streamed around the updraft perimeter in mid- to upper levels and beneath the anvil outflow and detrained some air from the weaker updraft perimeter. This airstream was essentially outside the dividing streamline between air within the updraft core and horizontal flow that stays essentially at the same altitude as it flows around the updraft core. This was especially true above the level where the updraft became divergent. Foote (1984) pointed to the convergent nature of the updraft in low levels and its divergent nature in the higher levels as the basic way air and millimeter-sized precipitation particles move toward and away from the updraft core.

We found that graupel and small hail could be grown from scratch from cloud droplet nucleation at cloud base, followed by freezing and continued growth aloft. However, particles smaller than a few millimeters were mostly exhausted into the eastward streaming anvil once the updraft strengthened during the mature phase. We were unable to demonstrate that the early horizontal flow out of the diverging updraft aloft did indeed carry any of these near-millimeter-sized particles westward from the updraft core. Reflectivity values around the west (upwind) side of the mid- to upper level, early

updraft were near -10 dBZ, which is much higher than might be expected if the radar echo was composed solely of small ice crystals and frozen cloud droplets with sizes of a few tens of microns. As the storm expanded in the mid- to upper levels, the likelihood of some millimeter-sized particles passing westward became more certain, likely a result of unresolved motions not present in the Doppler-derived winds.

The observed onsets of positive CG lightning and large hail as deduced with the hydrometeor identification algorithm and diagnosed with the precipitation growth model were essentially coincident in time. Trends in both hail echo volumes and positive CG lightning were found to closely follow the updraft surges, which will be discussed in more detail in Part II. Additionally, maxima in hail echo volume as measured by both the FHC and the particle growth model, resided between the melting level and the $-10°C$ level (5–7 km MSL) of the storm.

6. Conclusions

This study has shown that hail embryos can come from a much broader region than the so-called embryo curtain (BF76) as previously suggested by Nelson (1983). Smaller cells were observed upstream of the low-level inflow at two or three different times and could have contributed more embryonic particles that would have affected graupel and hail production. Our findings are also consistent with Foote's (1984) supposition that horizontally converging flow below the updraft maximum is the basic injection mechanism for transporting embryos into the updraft.

From the precipitation growth calculations, we have outlined four basic conditions that must be met in order for the storm to produce (large) hail: 1) small near-millimeter to millimeter-sized embryonic particles must be present, 2) there must be a mechanism for transporting these particles into the updraft, 3) the updraft must be of sufficient size and intensity to grow these embryonic particles into hail, and 4) the horizontal winds must keep the growing particles within favored hail growth conditions. In particular, strong updraft (>10 m s^{-1}) within a large fraction of the storm was required to produce any hail. A large region of cyclonically curved flow around the right flank of this updraft was apparently critical for the production of any hail larger than 20 mm. We conclude that, if these kinematic features are not present, a storm can only produce graupel particles with little or no hail.

REFERENCES

Bringi, V. N., and V. Chandrasekar, 2000: *Polarimetric Doppler Weather Radar: Principles and Applications.* Cambridge University Press, 636 pp.

——, K. Knupp, A. Detwiler, L. Liu, I. J. Caylor, and R. A. Black, 1997: Evolution of a Florida thunderstorm during the convection and precipitation/electrification experiment: The case of 9 August 1991. *Mon. Wea. Rev.,* **125,** 2131–2160.

Browning, K. A., 1964: Airflow and precipitation trajectories within severe local storms which travel to the right of the winds. *J. Atmos. Sci.,* **21,** 634–639.

——, 1977: The structure and mechanisms of hailstorms. *Hail: A Review of Hail Science and Hail Suppression, Meteor. Monogr.,* No. 38, Amer. Meteor. Soc., 1–43.

——, and G. B. Foote, 1976: Airflow and hail growth in supercell storms and some implications for hail suppression. *Quart. J. Roy. Meteor. Soc.,* **102,** 499–533.

Byers, H. R., and R. R. Braham, 1949: *The Thunderstorm.* U.S. Government Printing Office, 287 pp.

Carey, L. D., and S. A. Rutledge, 1996: A multiparameter radar case study of the microphysical and kinematic evolution of a lightning producing storm. *Meteor. Atmos. Phys.,* **59,** 33–64.

——, and ——, 1998: Electrical and multiparameter radar observations of a severe hailstorm. *J. Geophys. Res.,* **103,** 13 979–14 000.

——, and ——, 2000: The relationship between precipitation and lightning in tropical island convection: A C-band polarimetric radar study. *Mon. Wea. Rev.,* **128,** 2687–2710.

——, ——, D. A. Ahijevych, and T. D. Keenan, 2000: Correcting propagation effects in C-band polarimetric radar observations of tropical convection using differential propagation phase. *J. Appl. Meteor.,* **39,** 1405–1433.

Cifelli, R., W. A. Petersen, L. D. Carey, and S. A. Rutledge, 2002: Radar observations of the kinematic, microphysical, and precipitation characteristics of two MCSs in TRMM-LBA. *J. Geophys. Res.,* **107,** 8077, doi:10.1029/2000JD000264.

Conway, J. W., and D. S. Zrnic, 1993: A study of embryo production and hail growth using dual-Doppler and multiparameter radars. *Mon. Wea. Rev.,* **121,** 2511–2528.

Cummins, K. L., M. J. Murphy, E. A. Bardo, W. L. Hiscox, R. B. Pyle, and A. E. Pifer, 1998: A combined TOA/MDF technology upgrade of the U.S. National Lightning Detection Network. *J. Geophys. Res.,* **103,** 9035–9044.

Doviak, R. J., and D. S. Zrnic, 1993: *Doppler Radar and Weather Observations*. 2d ed. Academic Press, 562 pp.

Dye, J. E., B. E. Martner, and L. J. Miller, 1983: Dynamical–microphysical evolution of a convective storm in a weakly sheared environment. Part I: Microphysical observations and interpretation. *J. Atmos. Sci.,* **40,** 2083–2096.

Foote, G. B., 1984: A study of hail growth utilizing observed storm conditions. *J. Climate Appl. Meteor.,* **23,** 84–101.

——, and H. W. Frank, 1983: Case study of a hailstorm in Colorado. Part III: Airflow from triple Doppler measurements. *J. Atmos. Sci.,* **40,** 686–707.

Gal-Chen, T., 1982: Errors in fixed and moving frames of reference. Applications for conventional and Doppler radar analysis. *J. Atmos. Sci.,* **39,** 2279–2300.

Hall, M. P. M., J. W. F. Goddard, and S. M. Cherry, 1984: Identification of hydrometeors and other targets by dual-polarization radar. *Radio Sci.,* **19,** 132–140.

Herzegh, P. H., and A. R. Jameson, 1992: Observing precipitation through dual-polarization radar measurements. *Bull. Amer. Meteor. Soc.,* **73,** 1365–1374.

Hubbert, J., and V. N. Bringi, 1995: An iterative filtering technique for the analysis of copolar differential phase and dual-frequency radar measurements. *J. Atmos. Oceanic Technol.,* **12,** 643–648.

——, ——, L. D. Carey, and S. Bolen, 1998: CSU–CHILL polarimetric radar measurements from a severe hail storm in eastern Colorado. *J. Appl. Meteor.,* **37,** 749–775.

Illingworth, A. J., J. W. F. Goddard, and S. M. Cherry, 1987: Polarization radar studies of precipitation development in convective storms. *Quart. J. Roy. Meteor. Soc.,* **113,** 469–489.

Klemp, J. B., R. B. Wilhelmson, and P. S. Ray, 1981: Observed and numerically simulated structure of a mature supercell thunderstorm. *J. Atmos. Sci.,* **38,** 1558–1580.

Knight, C. A., and N. C. Knight, 1973: Hailstone embryos and hailstone models. Preprints, *Eighth Conf. on Severe Local Storms*, Denver, CO, Amer. Meteor. Soc., 77–79.

——, and K. Knupp, 1986: Precipitation growth trajectories in a CCOPE storm. *J. Atmos. Sci.,* **43,** 1057–1073.

Lang, T. J., and Coauthors, 2004: The severe thunderstorm electrification and precipitation study. *Bull. Amer. Meteor. Soc.,* **85,** 1107–1125.

Liu, H., and V. Chandrasekar, 2000: Classification of hydrometeors based on polarimetric radar measurements: Development of fuzzy logic and neuro-fuzzy systems and in situ verification. *J. Atmos. Oceanic Technol.,* **17,** 140–164.

Miller, L. J., J. E. Dye, and B. E. Martner, 1983: Dynamical–microphysical evolution of a convective storm in a weakly sheared environment. Part II: Airflow and precipitation trajectories from Doppler radar observations. *J. Atmos. Sci.,* **40,** 2097–2109.

——, C. G. Mohr, and A. J. Weinheimer, 1986: The simple rectification to Cartesian space of folded radial velocities from Doppler radar sampling. *J. Atmos. Oceanic Technol.,* **3,** 162–174.

——, J. D. Tuttle, and C. K. Knight, 1988: Airflow and hail growth in a severe northern High Plains supercell. *J. Atmos. Sci.,* **45,** 736–762.

——, ——, and G. B. Foote, 1990: Precipitation production in a large Montana hailstorm: Airflow and particle growth trajectories. *J. Atmos. Sci.,* **47,** 1619–1646.

Mohr, C. G., and R. L. Vaughn, 1979: An economical approach for Cartesian interpolation and display of reflectivity factor data in three-dimensional space. *J. Appl. Meteor.,* **18,** 661–670.

——, L. J. Miller, R. L. Vaughn, and H. W. Frank, 1986: On the merger of mesoscale datasets into a common Cartesian format for efficient and systematic analysis. *J. Atmos. Oceanic Technol.,* **3,** 143–161.

Moller, A. R., C. A. Doswell III, M. P. Foster, and G. R. Woodall, 1994: The operational recognition of supercell thunderstorm environments and storm structures. *Wea. Forecasting,* **9,** 327–347.

Nelson, S. P., 1983: The influence of storm flow structure on hail growth. *J. Atmos. Sci.,* **40,** 1965–1983.

——, 1987: The hybrid multicellular–supercellular storm—An efficient hail producer. Part II: General characteristics and implications for hail growth. *J. Atmos. Sci.,* **44,** 2060–2073.

O'Brien, J. J., 1970: Alternative solutions to the classical vertical velocity problem. *J. Appl. Meteor.,* **9,** 197–203.

Pruppacher, H. R., and J. D. Klett, 1997: *Microphysics of Clouds and Precipitation*. Kluwer Academic, 954 pp.

Rotunno, R., and J. B. Klemp, 1982: The influence of the shear-induced pressure gradient on thunderstorm motion. *Mon. Wea. Rev.,* **110,** 136–151.

Rust, W. D., and D. R. MacGorman, 2002: Possibly inverted-polarity electrical structure in thunderstorms during STEPS. *Geophys. Res. Lett.,* **29,** 1517, doi:10.1029/2001GL014303.

Ryzhkov, A. V., and D. S. Zrnic, 1998: Polarimetric rainfall estimation in the presence of anomalous propagation. *J. Atmos. Oceanic Technol.,* **15,** 1320–1330.

Smith, P. L., D. J. Musil, A. G. Detwiler, and R. Ramachandran, 1999: Observations of mixed-phase precipitation within a CAPE thunderstorm. *J. Appl. Meteor.,* **38,** 145–155.

Straka, J. M., E. N. Rasmussen, and S. E. Fredrickson, 1996: A mobile mesonet for finescale meteorological observations. *J. Atmos. Oceanic Technol.,* **13,** 921–936.

——, D. S. Zrnić, and A. V. Ryzhkov, 2000: Bulk hydrometeor classification and quantification using polarimetric radar data: Synthesis of relations. *J. Appl. Meteor.,* **39,** 1341–1372.

Wakimoto, R. M., and V. N. Bringi, 1988: Dual-polarization observations of microbursts associated with intense convection: The 20 July storm during the MIST project. *Mon. Wea. Rev.,* **116,** 1521–1539.

Weisman, M. L., and L. J. Miller, 2000: An overview of the severe thunderstorm electrification and precipitation study (STEPS). Preprints, *20th Conf. on Severe Local Storms*, Orlando, FL, Amer. Meteor. Soc., 654–656.

Wiens, K. C., S. A. Rutledge, and S. A. Tessendorf, 2005: The 29 June 2000 supercell observed during STEPS. Part II: Lightning and charge structure. *J. Atmos. Sci.,* **62,** 4151–4177.

Williams, E. R., 2001: The electrification of severe storms. *Severe Convective Storms, Meteor. Monogr.*, No. 50, Amer. Meteor. Soc., 527–561.